AMERICAN
METEOROLOGICAL
SOCIETY

*Journal of the Atmospheric Sciences*

**EARLY ONLINE RELEASE**

This is a preliminary PDF of the author-produced manuscript that has been peer-reviewed and accepted for publication. Since it is being posted so soon after acceptance, it has not yet been copyedited, formatted, or processed by AMS Publications. This preliminary version of the manuscript may be downloaded, distributed, and cited, but please be aware that there will be visual differences and possibly some content differences between this version and the final published version.

The DOI for this manuscript is doi: 10.1175/JAS-D-14-0130.1

The final published version of this manuscript will replace the preliminary version at the above DOI once it is available.

If you would like to cite this EOR in a separate work, please use the following full citation:

Xu, W., and S. Rutledge, 2014: Morphology, Intensity, and Rainfall Production of MJO Convection: Observations from DYNAMO Shipborne Radar and TRMM. J. Atmos. Sci. doi:10.1175/JAS-D-14-0130.1, in press.

© 2014 American Meteorological Society

Manuscript (non-LaTeX)
Click here to download Manuscript (non-LaTeX): XR14_JAS_2ndRevised.doc

# Morphology, Intensity, and Rainfall Production of MJO Convection: Observations from DYNAMO Shipborne Radar and TRMM

Weixin Xu and Steven A. Rutledge

Department of Atmospheric Science

Colorado State University, Fort Collins, Colorado

Submitted to:

*Journal of the Atmospheric Sciences*

DYNAMO/CINDY/AMIE/LASP Special Collection

Submitted: May 2014

Revised: September 2014

---

Corresponding Author Address: Weixin Xu, Department of Atmospheric Sciences, Colorado State University, 3915 West Laporte Avenue, Fort Collins, CO 80521.

Email: wxinxu@atmos.colostate.edu

PRELIMINARY ACCEPTED VERSION

# ABSTRACT

This study uses DYNAMO shipborne (R/V Revelle) radar and TRMM Precipitation Radar (PR) datasets to investigate MJO-associated convective systems in specific organizational modes (MCS vs. sub-MCS, linear vs. non-linear). The Revelle radar sampled many "climatological" aspects of MJO convection as indicated by comparison with the long-term TRMM PR statistics, including areal mean rainfall (6-7 mm $d^{-1}$), convective intensity, rainfall contributions from different morphologies, and their variations with MJO phase. Non-linear sub-MCSs were present 70% of the time but contributed just ~20% of the total rainfall. In contrast, linear and non-linear MCSs were present 10% of the time, but contributed 20% and 50%, respectively. These distributions vary with MJO phase, with the largest sub-MCS rainfall fraction in suppressed phases (phases 5-7) and maximum MCS precipitation in active phases (phases 2-3). Similarly, convective/stratiform rainfall fractions also varied significantly with MJO phase, with the highest convective fractions (70-80%) in suppressed phases and the largest stratiform fraction (40-50%) in active phases. However, there are also discrepancies between the Revelle radar and TRMM PR. Revelle radar data indicated a mean convective rain fraction of 70% compared to 55% for TRMM PR. We show this difference is attributed to the reduced resolution of the TRMM PR compared to the ship radar. There are also notable differences in the rainfall contributions as a function of convective intensity between the Revelle radar and TRMM PR. In addition, TRMM PR composites indicate linear-MCS rainfall increases after MJO onset and produces similar rainfall contributions to non-linear MCSs; however, the Revelle radar statistics show the clear dominance of non-linear MCS rainfall.

# 1. Introduction

The Madden-Julian Oscillation (MJO) (Madden and Julian 1971, 1972) is the most remarkable intraseasonal concept in the tropics. The MJO has broad impacts on the global weather and climate (Lau and Waliser 2005; Zhang 2005; Zhang 2013) such as monsoon onset and rainfall variability (Lau and Chan 1986; Hendon and Liebmann 1990; Lawrence and Webster 2002), tropical cyclone frequency (Liebmann et al. 1994; Maloney and Hartmann 2000), tornado outbreaks (Thompson and Roundy 2013), ENSO (Zhang 2005; Lau 2012), and extratropical climate modes (Lin et al. 2009; L'Herueux and Higgins 2008). Despite decades of study, the MJO is not well understood and therefore MJO prediction skill is limited, especially concerning initiation over the Indian Ocean (Bechtold et al. 2008; Kim et al. 2009; Vitart and Molteni 2010). Meanwhile, the MJO has been poorly simulated by several generations of general circulation models (GCMs) (Lin et al. 2006; Hung et al. 2013). To advance understanding of the oceanic and atmospheric processes governing MJO initiation, the Dynamics of the Madden-Julian Oscillation (DYNAMO) field campaign was carried out in the central Indian Ocean (CIO) region during boreal fall and winter of 2011/2012 (Yoneyama et al. 2013). DYNAMO deployed sounding networks, radars across a spectrum of wavelengths, aircraft, oceanographic instrumentation, and enhanced moorings (Yoneyama et al. 2013). One of the key DYNAMO hypotheses is that specific convective populations are essential to MJO initiation. DYNAMO is well suited for testing this hypothesis through providing continuous three-dimensional measurements of convective clouds, both precipitating and non-precipitating.

The DYNAMO field campaign observed three MJO events during the October 2011 – March 2012 time period (Yoneyama et al. 2013; Gottschalck et al. 2014). Observations from multi-wavelength and multi-platform (ground-based, shipborne, and airborne) radars have been used to investigate the full spectrum of convective clouds during these MJO events. Feng et al. (2014) constructed a merged cloud-precipitation radar dataset from three radars ($K_a$, C and S-band) deployed on Addu Atoll (Gan Is., Maldives) to document both precipitating (i.e., shallow, congestus, and deep convective clouds) and non-precipitating clouds (i.e., mid-level, cirrus, and anvil clouds). This dataset, together with radiosonde data, can effectively serve to study the role of shallow and congestus clouds in the initiation of the MJO (Feng et al. 2014). Based on S-band (S-pol) radar measurements collected during DYNAMO, Zuluaga and Houze (2013) found that rainfall in MJO active periods was intermittent and occurred in episodes lasting 2-4 days. They examined the convective population within these rainfall episodes, and showed that shallow convective echoes (SCE) and narrow deep convective cores (DCC), wide convective cores (WCC), and broad stratiform (BSR) systems were the most frequent prior to, during, and after the maximum rainfall, respectively. It is interesting that this convective transition pattern on the scale of 2-4 days is actually similar to that on the MJO scale observed by satellite remote sensing (Morita et al. 2006; Tromeur and Rossow 2010; Riley et al. 2011) and shipborne radar in DYNAMO (Xu and Rutledge 2014). In addition, convective systems in various stages of the MJO also exhibit different microphysical properties (Rowe and Houze 2014). Using the S-pol radar data, Powell and Houze (2014) found that precipitation area, radar echo-top height, and tropospheric humidity rapidly increase over ~3-7 days prior to the MJO onset. Based on shipborne radar measurements in DYNAMO, Xu and Rutledge (2014, hereafter XR14) documented a longer period of convective deepening prior to MJO onset, about 10-15 days. This longer convective deepening period is consistent with atmospheric moistening time scales inferred from the DYNAMO sounding network (Johnson and Ciesielski 2013). XR14 further composited the ship-based radar data as a function of MJO phase and identified strong correlations between convective populations and environmental conditions, both evolving along the “recharge”-“discharge” process (Blade and Hartmann 1993; Hu and Randall 1994; Kemball-Cook and Weare 2001). The precipitating cloud population consists of shallow isolated convective cells in suppressed phases, isolated deep convective systems two phases prior to MJO onset, deep organized MCSs in active MJO phases, and stratiform-dominant systems in decaying phases. Guy and Jorgensen (2014) also found similar shallow-to-deep-to-stratiform evolution of convective systems from analysis of airborne Doppler radar observations of the November MJO event during DYNAMO.

Although the above studies have extensively examined the convective and microphysical properties of convective clouds across the MJO life cycle, their convective organization and precipitation morphology (e.g., linear or non-linear, MCS or sub-MCS) have not been quantified. Convective organization has important effects on heating distributions, momentum transport, and surface fluxes. For example, squall lines accompanied by extensive stratiform precipitation have very different heating profiles from convective-only systems, as the corresponding latent heating profiles for the convective and stratiform components are distinctly different (Johnson 1984; Houze 1989; Tao et al. 1993). Previous studies have shown that convective momentum transport is a function of system organization, with up-gradient transport in the line-normal direction and down-gradient transport in the line-parallel direction (LeMone 1983; LeMone et al. 1984; Wu and Yanai 1994; Tung and Yanai 2002). Convection without linear organization does not show consistent momentum transport properties (LeMone 1983; LeMone et al. 1984). Furthermore, surface flux enhancement was observed to be much stronger in highly organized convective systems when linear squall lines proceeded a region of extensive stratiform precipitation (Saxen and Rutledge 1998).

Various organizational modes of tropical convection can occur under different environmental conditions, predominantly influenced by vertical shear and convective available potential energy (CAPE) (Moncrieff and Green 1972; Keenan and Carbone 1992; Lemone et al., 1998; Johnson et al. 2005). These studies found that vertical shear in the lower-to-middle troposphere is key to the orientation of convective lines while CAPE determines convective intensity and longevity. Convective systems can take on different morphologies, such as linear convection in the form of a leading convective line with trailing stratiform precipitation (e.g., Houze, 1977; Zipser, 1977) or randomly distributed convective cells. There are many studies on the convective organization and environmental characteristics in the literature, based on observations from the GARP Atlantic Tropical Experiment (GATE, Cheng and Houze 1979; Barnes and Seickman 1984; Szoke and Zipser 1986), the Tropical Ocean Global Atmosphere Coupled Ocean-Atmosphere Response Experiment (TOGA-COARE, LeMone 1983; LeMone et al. 1998; Rickenbach and Rutledge 1998), the South China Sea Monsoon Experiment (Johnson et al. 2005), the Equatorial Mesoscale Experiment (Alexander and Young 1992), and experiments in Northern Australia (Keenan and Carbone 1992; Keenan and Rutledge 1993). Recently, Liu and Zipser (2013) constructed a climatology of MCS morphology in the tropics and subtropics using 14 years of Tropical Rainfall Measuring Mission (TRMM) measurements. However, there are very limited studies focusing on the morphology of the MJO convection over the CIO where most MJOs initiate.

Zuluaga and Houze (2013) have examined the frequency of convective systems during the MJO active periods during DYNAMO with the organization of SCE, DCC, WCC, and BSR (previously defined). Guy and Jorgensen (2014) have investigated the convective organization and dynamics using airborne radar data collected from the NOAA P-3 aircraft deployed in DYNAMO. They found that DYNAMO MCSs were organized more parallel to the low-level shear and produced weaker cold pools due to weaker updrafts compared to MCSs observed in TOGA-COARE. However, the NOAA P-3 data were only available for a single MJO event (November) and nine separate flight episodes, therefore samples of convection were relatively limited (Guy and Jorgensen 2014). Despite this research, outstanding questions remain regarding convective organization and precipitation morphology over the CIO. For example the relative frequency of non-MCS versus MCS scale systems has not been quantified. Nor has the degree of convective organization (linear versus non-linear). Nor has the rainfall production by various convective modes. Collectively, the variability of these characteristics with MJO phase has also not been quantified. This study seeks to contribute knowledge in these areas. In addition, the DYNAMO-based analyses are placed in the context of the long-term satellite (i.e., TRMM) climatology. This study first describes a time series of precipitation morphology based on analysis of DYNAMO shipborne C-band radar measurements collected from the R/V *Roger Revelle*. DYNAMO observations are composited as a function of MJO phase, and compared in detail to the convective climatology based on TRMM PR data.

## 2. Data and Methodology

This study employs 15 years (1998-2012) of TRMM precipitation feature (PF) data (Liu et al. 2008) and 3 months (Oct-Dec, 2011) of radar observations collected from the research vessel (R/V) *Roger Revelle* deployed during DYNAMO (Moum et al. 2014). The long-term TRMM PR statistics cover the main MJO time period (October to April) over a $10^o$x$10^o$ box centered on the DYNAMO array (75° – 85° E; 5° S – 5° N). DYNAMO radar measurements are compared to the TRMM PR climatology from various perspectives, including convective organization, intensity, and rainfall production as a function of MJO phase.

## *a. TRMM data*

### 1) TRMM 3B42 rainfall product

The version 7 TRMM Multisatellite Precipitation Analysis (TMPA) 3B42 rain product (Huffman et al. 2007) is used to provide continuous rainfall time series and large-scale rainfall maps, since the TRMM satellite data are only available twice a day. The TMPA 3B42 data are available from 1998 to present, from 50 S to 50 N. This dataset has 3-hour temporal resolution and $0.25^{o}$ spatial resolution, and uses TRMM PR observations, passive-microwave measurements from low-earth orbit satellites, infrared radiance measurements from geostationary satellites, as well as rain gauge data when available.

### 2) TRMM PF dataset

We use the version 7 TRMM database, mainly observations from the precipitation radar (PR) (Kummerow et al. 1998), to provide climatological context for the DYNAMO ship radar data. PR measurements have been grouped into precipitation features (PFs) at the University of Utah (Liu et al. 2008). By definition, PFs are identified as PR-derived near-surface raining clusters (or continuous radar pixels). The minimum detectable reflectivity of the PR is 17 dBZ (Kummerow et al. 1998), which therefore defines the echo boundary of PFs (Fig. 1a). After a PF is identified, three-dimensional PR observations within the column are grouped into the PF, including such variables as maximum 20/30/40 dBZ echo-top heights, rainfall volume (2A25, Iguchi et al. 2009), convective and stratiform precipitation fractions (2A23, Awaka et al. 2009), and the overall precipitation area of the PF. Since the horizontal resolution of the PR is 4 km prior to orbit boost (August, 2001) and 4.5 km after boost, this study includes only PFs greater than 100 km$^2$ (4-5 TRMM PR pixels).

### *b. DYNAMO R/V Revelle dataset*

The R/V *Roger Revelle* (Moum et al. 2014) was deployed at the central east site (0 N, 80.5 E) of the DYNAMO sounding array over the CIO (Yoneyama et al. 2013). During DYNAMO, R/V *Revelle* made four cruises to the campaign area (Xu and Rutledge 2014) from September 2011 to January 2012. This study only analyzes measurements taken from cruises 2, 3, and 4 during which time the DYNAMO observations were extensive and MJO events were sampled (Yoneyama et al. 2013). Data are not included when the ship was transiting to/from port, or otherwise off station. The vacancy of the *Revelle* had little influence on our results, since (fortunately) most of the missing data periods occurred during suppressed MJO phases with little if any rainfall. TRMM 3B42 rainfall time series over our analysis period are virtually identical, when including and excluding data during the off station periods (XR14).

#### 1) Radar data

The NASA TOGA C-band radar onboard the R/V *Revelle* (hereafter called the Revelle radar) operated round the clock when the ship was on station (XR14). The Revelle radar completed a full volume scan every 10 minutes including 22 360$^{o}$ PPI (plan position indicator) sweeps and 5 vertical cross sections (RHI, range height indicator). This particular scanning strategy was set to provide continuous volume coverage and high-resolution 3-D precipitating cloud structure information (XR14). The Revelle radar data were calibrated and quality controlled by the Radar Meteorology Group at Colorado State University and NASA (details in XR14). After quality control, radar polar coordinate data were interpolated to Cartesian coordinates using the NCAR REORDER software package (Oye and Case 1995), with the resolution of 2 km in the horizontal and 0.5 km in the vertical (XR14). Radar reflectivity was then classified into convective and stratiform precipitation components based on Steiner et al. (1995). This algorithm only considers the horizontal texture of the radar reflectivity. Note that TRMM PR (2A23, Awaka et al. 2009) uses a somewhat more complicated technique that considers both horizontal and vertical gradients of reflectivity, as well as the existence of a reflectivity bright band. The Z-R relationship for convective rain is $Z=134R^{1.44}$. For stratiform rain, $Z=300R^{1.55}$ is used. These Z-R relationships (as well as the C-band attenuation correction algorithm) were derived from drop size distribution measurement on Gan Is. (DYNAMO) and Manus Is. in the western Pacific (Thompson et al. 2014). Echo top heights of specific echo intensities (e.g., 0 and 20 dBZ) are obtained by finding the maximum height of that value in the particular grid point column.

### 2) Radar-based PFs

The echo object identification method used in the TRMM PF (Nesbitt et al. 2000; Liu et al. 2008) study was applied to the entire Revelle radar dataset. Specifically, radar PFs are defined as contiguous radar pixels exceeding the minimum TRMM PR detectable reflectivity (17 dBZ) at 2-km altitude (Fig. 1b). As a particular example, the Revelle radar observed nearly the same PF pattern as the TRMM PR (Fig. 1a-b). The three-dimensional radar measurements within the column are grouped into the PF. Therefore, radar PFs contain parameters such as maximum height of specific radar reflectivities (e.g. 20 or 30 dBZ), feature size (area of pixels > 20 dBZ), as well as intensity, area, and volume of convective and stratiform precipitation. Again, radar PFs smaller than 100 km$^2$ (same rule applied to TRMM PFs) were not considered for analysis.

### *c. PF morphologies*

The goal of this study is to quantify the frequency, intensity, and rainfall contributions of the MJO associated convective systems as a function of convective organization (morphology). Rickenbach and Rutledge (1998, hereafter RR98) described the morphology of convection over the western Pacific warm pool using observations collected from the MIT C-band radar onboard the R/V *John V. Vickers* deployed during TOGA-COARE. RR98 divided echoes by sub-MCS versus MCS scales (less than or exceeding a length scale of 100 km), and whether the convective component was organized in a linear or non-linear manner. We utilize a similar classification here. RR98 only assigned one organizational mode per radar volume, that being the mode with the largest size (MCS) and the highest degree of organization (linear). In contrast, this study utilizes an algorithm to automatically classify each PF, allowing multiple modes per radar volume. The algorithm applies elliptical fits to the area of PFs and calculates dimensions (e.g., major and minor axes) of the ellipses (Nesbitt et al. 2006; Liu and Zipser 2013). The major and minor axis lengths of the ellipse are derived from the mass distribution tensor eigenvalues of the raining points within each feature (Medioni et al. 2000; Nesbitt et al. 2006). First of all, PFs are separated into MCSs (area > 1000 km$^2$) and sub-MCSs (area < 1000 km$^2$) mainly following the TRMM PR morphology studies (Nesbitt et al. 2000; Cifelli et al. 2007; Liu et al. 2008; Liu and Zipser 2013). This 1000 km$^2$ area scale threshold for the MCS category actually produces very similar MCS rainfall statistics (< 10% difference) as the 100 km horizontal scale used by RR98 (not shown). MCSs and sub-MCSs are further defined as linear or non-linear depending on the ratios of major to minor axes associated with each PF. RR98 defined the major-to-minor ratios of convective features (only considering convective components) > 5:1 as linear and ratios < 5:1 as non-linear. However, we define the major-to-minor ratios of PFs > 5:2 as linear and ratios < 5:2 as non-linear, considering that PFs (or precipitating area) are much broader than the embedded convective elements. Liu and Zipser (2013) also pointed out that the linear convection definition (ratios < 5:1) is too restrictive for PFs. Sensitivity tests show that difference in rainfall statistics of linear or non-linear MCSs is about 10% between the major-to-minor ratios of 5:1 and 5:2 definitions. Figs. 1c-d provide examples of radar PFs in different morphology categories. Linear MCSs generally represent squall-line systems or convective cells arranged in a linear fashion (Fig. 1c), while non-linear MCSs have randomly distributed cells embedded within stratiform precipitation (Fig. 1d).

### *d. MJO indices*

This study employs the Wheeler–Hendon Real-Time Multivariate MJO (RMM) index (Wheeler and Hendon 2004, hereafter WH index) to define the MJO phase. The WH index is based on the combined empirical orthogonal functions (EOFs) of outgoing longwave radiation (OLR) and zonal wind fields at 850 and 200-hPa. The WH index has been widely used and is an effective filter for intraseasonal frequencies associated with the MJO (Wu and Lau 2010; Riley et al. 2011). Based on the WH index, each day in the tropics can be assigned to one of eight MJO phases. The active MJO phases over the CIO are assigned as phases 2 and 3. In other words, phases 1 and 4 correspond to pre-onset and post MJO periods in the CIO, while phases 5-8 are associated with suppressed MJO activity over this same domain. During the three MJO events in

DYNAMO (October-December, 2011), most of the days were of relatively strong MJO magnitude ($RMM1^2 + RMM2^2 > 1$), indicating significant MJO events (XR14). On the other hand, there were more than 50 MJO events observed by the TRMM satellite from October to April during 1998-2012. In compositing TRMM data as a function of MJO phase, we only include TRMM measurements taken during significant MJO periods (i.e., $RMM1^2 + RMM2^2) > 1.2$.

## 3. Convective Evolution of MJOs during DYNAMO

The DYNAMO field campaign observed two coherent MJO events and one incoherent (with incomplete cycle) MJO event (Yoneyama et al. 2013; Gottschalck et al. 2014; Johnson and Ciesielski 2013). The two coherent MJOs occurred in October (MJO 1) and November 2011 (MJO 2) with convection propagating from the CIO to the central Pacific and wind signals circumnavigating the globe (Gottschalck et al. 2014). Figure 2 clearly shows that the MJO heavy precipitation envelope initiated over the western Indian Ocean (Fig. 2a and d), passing through the DYNAMO array (Fig. 2b and e), and propagating eastward to the Maritime Continent (Fig. 2c and f). The prolonged rain event observed by the Revelle radar during MJO 1 (Fig. 2a-c) was associated with the most intense portion of that particular MJO event. During MJO 2 (Fig. 2d-f), although intense precipitation was observed by the Revelle radar (Fig. 2e), the strongest convection and precipitation occurred over the northern portion of the large scale DYNAMO array (Fig. 2e). The December MJO (MJO 3) was weaker in the OLR field accompanied by less coherent propagation in the wind component (Gottschalck et al. 2014). Only decaying phases (e.g., WH phases 4-5) were observed in MJO 3 as the more intense convection was located north of the Revelle radar coverage area (not shown).

Figure 3 shows time series of Revelle radar-estimated rainfall (3 hourly, areal mean) as a function of convective morphology during MJO 1 (Fig. 3a) and MJO 2 (Fig. 3b). [Due to the nature of the sampling for MJO 3, we do not consider MJO 3 for this time series analysis, however we do include MJO 3 in the precipitation statistics described in more detail later.] The WH phase for each MJO is indicated at the top of each time series panel. In general, suppressed periods (phases 5-7) in both MJO events were dominated by precipitation from sub-MCSs. During active periods (phases 2-3), frequent MCS (both linear and non-linear) precipitation was present. These results are consistent with the evolution of precipitating cloud populations described by XR14. XR14 showed that deep convective cells frequently developed prior to MJO onset (i.e., during phase 1), but those cells rarely organized into mesoscale systems. Throughout the MJO cycle, sub-MCSs make minor contributions to precipitation (areal mean, 2-10 mm $d^{-1}$), roughly 5-10% of that generated by MCSs (areal mean, 30-80 mm $d^{-1}$). However, sub-MCSs (or isolated convective cells) dominate the convective cloud population during DYNAMO and were suggested to play an important role in moistening the lower troposphere during MJO "recharging" periods (XR14). In terms of organizational mode, non-linear MCSs contributed the most rainfall (20-60 mm $d^{-1}$), while linear MCSs produced only 20-30% of that of the non-linear MCSs (< 25 mm $d^{-1}$).

During MJO active periods, MCS precipitation was more frequent and of higher intensity in MJO 1 than MJO 2 (Fig. 3, Table 1). As a result, the MJO envelope (active period) contained substantially more rainfall in MJO 1 (13.7 mm $d^{-1}$) compared to MJO 2 (9.3 mm $d^{-1}$, Table 1). This is also evident from the rainfall maps shown in Figs. 2b and d. There were more than 10 major MCS precipitation events in MJO 1 (Fig. 3a). In MJO2, there were only two major periods of MCS precipitation during active phases (Fig. 3b). These MCS precipitation events were associated with the passage of two Kelvin waves comprising MJO 2 (Nov. 24 and Nov. 28; Gottschalck et al. 2014; Moum et al. 2014). Indeed, the precipitation morphology depicted here follows the evolution of echo-top height (0 dBZ radar echo-top) as shown by XR14 (their Fig. 3b). For example, precipitating echo tops became substantially deeper around Oct. 16 in MJO 1 and Nov. 21 during MJO 2, when the dominant convective mode shifted to MCS precipitation (Fig. 3). This is reasonable since deep convective cells are necessary for MCS development. Prior to MJO onset, convective deepening (increase of the echo-top height) was more persistent and substantial in MJO 1 than MJO 2 (XR14). After the MJO onsets, MCSs were more frequent and contributed more rainfall in MJO 1 than MJO 2 (Fig. 3, Table 1).

## 4. Overall DYNAMO Radar Statistics and TRMM Climatology

Based on echo object (or PFs) analysis, convective characteristics derived from 3-months of Revelle radar measurements are placed in the context of a 15-yr TRMM climatology (October-April) over the CIO (5°N-5°S, 75°-85°E; white box in Fig. 2). As detailed below, the 3 month long Revelle radar-observed precipitation feature populations for the MJO's sampled during DYNAMO closely resemble the precipitation feature populations found in the TRMM PR 15 year climatology (Table 2), comprised of over 50 individual MJO events between 1998-2012. The 3-month areal mean rainfall rate recorded by the Revelle radar (7.0 mm $d^{-1}$) was also very close to that of the TRMM PR's 15-yr climatology (6.1 mm $d^{-1}$), which is also consistent with that derived from the multi-satellite rainfall product (3B42, 6.6 mm $d^{-1}$). It is interesting that DYNAMO recorded much higher daily rainfall compared to TOGA COARE (radar estimates of

4.5-4.8 mm d$^{-1}$, Short et al. 1997; RR98). This difference may owe to the fact that only one major MJO event occurred during TOGA COARE, while DYNAMO observed three MJO events during its (similar) duration. In fact, the 15-yr averaged areal rainfall rate based on TRMM PR centered on the TOGA COARE large-scale domain (5S-5N; 140-150 E) is 6.7 mm d$^{-1}$, very similar to that of DYNAMO. TRMM PR and the Revelle radar also observed very similar convective precipitation areas (25-27%). However, there is a significant discrepancy concerning the convective rain volume fraction between TRMM PR (55%) and Revelle radar (73%). In fact, the convective rain fraction derived from Revelle radar (73%) is very close to that based on TOGA COARE shipborne radars (72%; Short et al. 1997; RR98). In contrast, Lin et al. (2004) reported a convective rain fraction of 40-50% (or stratiform rain of 50-60%) over the equatorial tropics based on a 5-yr TRMM PR climatology. The reason that the TRMM PR convective fraction is less than Revelle is due to the reduced resolution of the TRMM PR. For example, the convective /stratiform fractions become 60/40 percent when the Revelle radar data are reduced to a 4 km resolution. The coarser resolution of the TRMM PR relative to the Revelle radar does not allow it to resolve various reflectivity gradients that are characteristic of convection. We also need to emphasize that the convective-stratiform fractions derived from the Revelle data may not be generally representative of MJO precipitation since only MJO 1 made a "direct hit" on the *Revelle's* location (Fig. 2), with the heaviest precipitation passing to the north of the Revelle during MJO 2 and 3.

### *a. Morphology statistics*

Even though the MJOs documented during DYNAMO passed through the Revelle radar area to various degrees, the distribution (CDF) of Revelle radar PFs as a function of size is very close to that of the TRMM PR climatology (Fig. 4, red curves). This agreement suggests that during the 3-month observational period the Revelle radar did obtain a view of MJO convection that is representative of MJOs over this region of the CIO. Recall that the TRMM PR database contains over 50 MJO events. Although MCSs (PFs > 1000 km$^2$) comprise only 10% of the total PF population, they contribute more than 70% of the total precipitation (Fig. 4, blue curves). This is quite common over the tropics (Nesbitt et al. 2000; Liu et al. 2008; Cifelli et al. 2007). Compared to the TRMM PR, the Revelle radar observed a smaller fraction of rainfall contributed by very large PFs (> 50,000 km$^2$). This may be due to the fact that the TRMM PR simply covers a larger swath area compared to the Revelle radar.

Figure 5 shows the PF frequency, contribution to total rainfall, and convective rain fraction in the four morphology categories. Error bars represent T test at the 95% significance level. Generally, the TRMM PR climatology and the Revelle radar statistics show similar distribution patterns as a function of PF morphology. They both indicate significant differences among different morphologies. The occurrence frequency (green bars in Fig. 5) is in the ascending order of linear MCSs (3-5%), non-linear MCSs (5-7%), linear sub-MCSs (20-25%), and non-linear sub-MCSs (60-65%). Obviously, the non-linear sub-MCS mode dominated over the CIO in terms of frequency of occurrence. The linear MCS category was the least observed convective mode. In terms of rainfall contribution (blue bars in Fig. 5), non-linear MCSs contributed ~50% of the total rainfall, compared to linear MCSs which produced ~20% of the total rainfall. Similarly, sub-MCSs with linear organization contributed less rain (< 10%) than non-linear sub-MCSs (~20%). RR98, examining TOGA COARE shipborne radar data, reported that MCSs with linear organization dominated the total rainfall (80%), while non-linear MCSs contributed less than 5% of the total rainfall. However, this study is PF-based (multiple categories can appear in one radar image), while RR98 manually defined each radar image as having only one morphology mode defined as the convective feature with the highest degree of organization and size (i.e., the linear MCS is the largest and most organized mode). This study utilizes an objective algorithm (Nesbitt et al. 2006; Liu and Zipser 2013) to automatically identify each PF as one of the morphology categories, allowing systems of different morphologies (e.g., MCS and isolated convective cells) to be classified within the same radar image. In addition, RR98 classified on only convective components, while this study classifies on overall precipitation area of PFs. In fact, our analysis method yields very similar statistics when it is applied to the TOGA COARE MIT radar data (RR98) and TRMM PR measurements over a box of 1000 km by 1000 km over the TOGA COARE region (Fig. 6). Furthermore, our morphology statistics are consistent with the TRMM PR climatology across the broad tropical oceans, e.g., there were three times more MCSs (PFs > 1000 km$^2$) in the non-linear mode compared to the linear mode (Liu and Zipser 2013). The assumptions made by RR98 (owing to the non-existence of automated methods to objectively evaluate the large amount of radar data) led to a bias towards linear MCS systems.

The convective rainfall fraction was also calculated for each morphology category (red bars in Fig. 5). Concerning the statistics derived from the Revelle radar, sub-MCSs have larger fractions of convective precipitation (85-95%) than MCS categories (60-85%), indicating the more isolated and convective nature of the former category. The lower fraction of convective rain in MCSs is of course due to their substantial stratiform precipitation component. The convective rain fraction in DYNAMO MCS events ranges from 70-85% for linear MCSs to 60-75% for non-linear MCSs. RR98 found an opposite trend for TOGA COARE event, with 66% for linear MCSs and 83% for non-linear MCSs. Collectively the convective fractions of

DYNAMO events are also somewhat higher than several case studies of individual tropical squall lines from GATE (Houze 1977, 60%; Gamache and Houze 1983, 51%; Houze and Rappaport 1984, 58%). The comparison of these statistics needs to be done with caution since different analysis techniques were used (including different Z-R relationships for convective and stratiform rain; different convective-stratiform partitioning assumptions, etc.). Also the present study represents a combination of many snapshot observations of MCS events while previous studies examined the entire life cycle of MCS events. Tropical squall lines over a portion of the system's lifetime produced a broad range of convective rain fractions (Leary 1984, 70%; Zipser et al. 1981, 45%–50%).

It is important to point out that there are also differences in the morphology statistics between TRMM PR and the Revelle radar. For example, linear MCSs have higher rainfall contributions based on TRMM PR (28%) compared to the Revelle radar (15%). This may be partially due to the fact that the TRMM PR can detect longer line-shaped PFs (i.e., maximum of 1000 km along the PR swath in the study box) compared to the Revelle radar (i.e., maximum dimension of 300 km). As shown in Fig. 4, the TRMM PR observed a larger fraction of rainfall from extremely large PFs. On the other hand, the Revelle radar detected a larger rainfall fraction contributed from non-linear sub-MCSs (23%) compared to 12% by TRMM PR. This may be due to the coarser native horizontal resolution of the TRMM PR data compared to the Revelle radar (4 km vs. ~2 km). Furthermore, the convective rain fraction based on the Revelle radar is higher than that of the TRMM PR climatology regardless of morphology category. Again, differences in the native data resolution are likely at play in explaining these differences.

### *b. Convective intensities*

Figure 7 shows the distribution (PDF) of 20/30 dBZ echo-top heights by convective mode, an indication of convective intensity. Revelle radar statistics are generally consistent with the TRMM PR climatology on echo-top heights of both the 20 and 30 dBZ, with Revelle-observed PFs slightly taller (0.5 km) than those measured by TRMM PR. It is clear that MCSs persistently exhibited higher 20 or 30 dBZ echo tops than sub-MCSs, indicating they contained stronger convective elements compared to convective elements in sub-MCSs. Rowe and Houze (2014) showed similar differences between MCSs and sub-MCSs over Gan Is. during DYNAMO, in terms of 0 dBZ echo tops and frequency of large ice particles deduced from the NCAR S-pol radar polarimetric data. Liu and Zipser (2012) reported that organized convective lines across the broad tropics are slightly weaker than those with near-circular shapes, indicated by lower 30 dBZ echo top heights and warmer 37 GHz brightness temperatures. However, this study indicated that convective systems over the CIO with linear and non-linear organization have nearly the same convective intensities (e.g., 30 dBZ echo-top heights). In this study, the 20 dBZ echo-top heights of MCSs peaked at 7.5 km, with approximately 10% of those systems achieving heights above 10 km (Fig. 7a). For MCS convective cores, the 30 dBZ echo-top height mode was near 6 km, with a very sharp drop off above this altitude (Fig. 7b). Only 5% of the 30 dBZ echo tops exceeded 8 km, which is an effective threshold for lightning occurrence (Zipser 1994; Petersen et al. 1996; Liu et al. 2012).

Figure 8 depicts rainfall fractions contributed by each morphology type as a function of 20/30 dBZ echo-top height. Most of the MCS rainfall (70-80%) was contributed from deep systems (e.g., 20 dBZ echo-top height > 10 km, Fig. 8a). Note that only 10% of the observed MCSs had 20 dBZ echo tops exceeding 10 km (Fig. 7a). Only 5% of the sub-MCS precipitation came from systems with 20 dBZ echo tops higher than 10 km. Approximately 10-20% (2%) of

MCS (sub-MCS) rainfall over the CIO was associated with intense convection, e.g., 30 dBZ echo-top > 8 km (Fig. 8b). Xu and Zipser (2012) reported that over oceans less than 10% of rainfall was contributed by intense convection (e.g, 30 dBZ echo tops > 8 km, or presence of lightning) compared to 70% over tropical continents. These findings are consistent with observed lightning frequencies presented by XR14.

There are notable differences in the rainfall contributions (as a function of convective intensity) between the Revelle radar and the TRMM PR climatology. The TRMM PR climatology suggests that more than 40% of the MCS rainfall was contributed by systems with extremely deep convective cores (e.g., 20 dBZ echo-top > 12 km), but the Revelle radar indicates only ~15% of MCS rainfall was due to MCSs with deep convective cores (Fig. 8a). In addition, TRMM PR climatology shows 20% of the MCS rainfall was associated with intense convection (30 dBZ echo-top > 8 km), while the Revelle radar shows only 10%. However, there was a larger fraction of sub-MCS rainfall contributed by PFs with relatively high echo tops (e.g., 20 dBZ echo-top > 8 km, or 30 dBZ echo-top > 6 km) as indicated by the Revelle radar compared to the TRMM PR climatology. Again, these discrepancies might originate from differences in rainfall estimation algorithms between TRMM PR and the Revelle radar, as the convective intensities are similar between Revelle statistics and TRMM PR climatology. It is possible that the TRMM PR underestimated rainfall for relative weak radar echoes but overestimated for strong radar echoes compared to the Revelle radar, since sub-MCSs should contain weaker radar echoes near the surface, due to their substantially weaker convective intensities compared to MCSs (Fig. 7).

## 5. Composites as a Function of MJO Phase

XR14 showed that convective characteristics (i.e., precipitation amount, convective intensity, and lightning frequency) and environmental variables (SST, tropospheric humidity) evolved along the “recharge”-“discharge” processes (Blade and Hartmann 1993; Kemball-Cook et al. 2001). One of the major goals of this study is to examine how the precipitation morphologies vary with MJO evolution, or MJO phase defined by the WH index. It is also important to know whether these MJO phase-based composites observed during DYNAMO are comparable to the TRMM PR climatological patterns. This section compares the three MJO events in DYNAMO against more than 50 MJO events observed by TRMM, from the perspectives of total rainfall, convective/stratiform rain fraction, precipitation morphology, and rainfall contribution as a function convective depth. There were more than 300 MJO event days in each MJO phase during October to April in 1998-2012. However, we only include major MJO event days (i.e., $RMM1^2 + RMM2^2) > 1.2$. Samples of selected MJO event days in each MJO phase and corresponding PF populations are listed in Table 3.

### *a. Total rainfall and precipitation types*

Figure 9 shows the areal mean rainfall derived from the Revelle radar, TRMM PR, and 3B42 estimates as a function of MJO phase. XR14 previously showed that Revelle radar-based rainfall time series agreed well with that from TRMM 3B42. Figure 9 indicates that the large-scale MJO phase-to-phase rainfall evolution pattern was also captured by the Revelle radar observations. For example, each rainfall plot shows a similar increasing trend from phase 7 to phase 2, maximum at phase 2, and a decreasing trend from phase 2 to 5. The MJO phase-composited rainfall evolution during DYNAMO (black, orange, and blue curves, Fig. 9) was higher than that of the TRMM PR climatology (red curve), especially during active phases of the

MJO (e.g., phases 1-3). Note that because the TRMM PR provides very small data samples during the 3 months of DYNAMO (only two overpasses per day), 3B42 data is used to represent the satellite rainfall estimates during DYNAMO. Compared to the 3B42 product over the Revelle radar coverage area (orange curve), the Revelle radar (black curve) measured more rainfall during MJO building phases (e.g., phases 8-1) but less rainfall during MJO active and decaying phases (phases 2-4). This may result from the fact that TRMM 3B42 mainly relies on microwave and Infrared measurements. Both microwave and Infrared rainfall estimation techniques are based on indirect relationships between ice particles/cloud tops and the surface precipitation that vary greatly among different weather regimes. During the active and decaying phases, precipitation systems could still have abundant ice particles and extensive cold cloud tops, but precipitation intensity is substantially reduced due to the weakening of convective intensity (Xu and Rutledge 2014). In this case, microwave/IR techniques likely overestimate precipitation. These trends suggest that 3B42 may underestimate rainfall produced by deep isolated convective cells during MJO building phases, and overestimate precipitation produced by large MCSs during active phases. Compared to 3B42 over the large-scale area (blue curve), the Revelle radar (black curve) diagnosed less rainfall during MJO active and decaying phases. This difference is likely caused by the heaviest precipitation passing to the north of the Revelle during MJO 2 and 3. However, the main take away message from the above is that the Revelle radar measurements evidently captured the MJO rainfall evolution revealed in the much longer record (TRMM PR) satellite statistics.

The total rainfall was further divided into convective and stratiform types based on estimations from the Revelle radar and TRMM PR (Fig. 10). The 3-month Revelle radar estimates (Fig. 10a) show similar rainfall magnitudes as the long-term TRMM PR estimates (Fig.

10c) but display greater phase-to-phase variability compared to TRMM PR climatology. Both Revelle (Fig. 10a-b) and TRMM PR (Fig. 10c-d) precipitation estimates show that convective precipitation dominates the suppressed MJO phases (phases 5-7), but stratiform type rainfall becomes substantial (40-50%) in the MJO active phases (phases 2-3). XR14 related the growth of stratiform precipitation to moist mid-to-upper tropospheric conditions and strong deep tropospheric wind shear in active MJO phases. Revelle radar observations indicate that 80-90% of the total precipitation in MJO suppressed phases (phases 5-7) falls as convective rain (Fig. 10b). This is reasonable, as the MJO suppressed phases were characterized by shallow and isolated convection as shown by XR14. In contrast, the TRMM PR climatology displays much lower convective rain fraction (50-60%) in the suppressed phases (Fig. 10d).

Throughout the MJO life cycle, TRMM PR estimated lower convective rain fractions compared to Revelle radar. As has been mentioned previously, this is mainly due to the coarser resolution of the TRMM PR (4 km) relative to the Revelle radar (~2 km) such that the TRMM PR cannot adequately resolve various reflectivity gradients that are often characteristic of convection. Sensitivity tests show that the convective rain fractions are similar between Revelle radar and TRMM PR when the Revelle radar data are degraded to 4 km resolution. In addition, the TRMM PR may classify some of the isolated convection as stratiform precipitation due to its lower sensitivity and reduced horizontal resolution compared to the Revelle radar. In fact, the identification of isolated convection poses a significant difficulty for partitioning algorithms (both for satellite and ground based radars) because these echoes often have low reflectivities and weak horizontal gradients. While these isolated echoes are minor contributors to the total rainfall (~10%), it is important to properly classify them in order to understand the role of shallow isolated convection in MJO initiation. These types of echoes are present in 20-30% of the radar observations from Revelle and are dominant during highly suppressed periods (XR14).

### *b. Rainfall distribution as a function of morphology and echo-top height*

The total precipitation in each MJO phase was also broken down into fractional rainfall contributed from PFs in each of the four morphologies (Figure 11). In general, suppressed MJO phases (e.g., phases 5-7) were characterized by sub-MCS rainfall, while active phases (e.g., phases 2-3) were dominated by the MCS rainfall. This is especially obvious in both the time series (Fig. 3) and composites (Fig. 11a-b) of Revelle radar measurements. Revelle-based composites also display more variability than the TRMM PR climatology. For example, Revelle radar measurements indicated 60-80% of the rainfall during suppressed phases (e.g., phases 5-7) came from sub-MCSs (Fig. 11b), while the TRMM PR analysis shows that only 30-40% of rainfall fell from sub-MCSs (Fig. 11d). Revelle-based composites also show that the increase of MCS precipitation was quite sudden, e.g., rapid increase from phases 7-8 to phase 1 (Fig. 11a; also see the time series of the two MJO events shown in Fig. 3). Both the Revelle radar and TRMM PR indicated that MCSs contribute 75-85% of the total precipitation during the MJO peak phase (e.g., phase 2, Fig. 11b and d). For active phases, TRMM PR climatology reveals that linear MCSs and non-linear MCSs each contribute significantly to total rainfall (~40%, Fig. 11d). Revelle radar measurements indicate dominance of non-linear MCS rainfall (~60%, Fig. 11b). The TRMM PR climatology also shows an increase of rainfall produced by linear MCSs from inactive to active phases (Fig. 11c-d), suggesting the frequent development of squall line systems during active periods. As has been previously mentioned, the long swath (up to 1000 km in the study box) of the TRMM PR might enable PR to detect longer (or larger) squall-line systems compared to the Revelle radar (whose coverage was limited to 300 km in length).

Figure 12 indicates the rainfall amount and fractions in each MJO phase contributed from PFs with different echo-top heights, i.e., shallow < 5 km, mid-depth 5-8 km, and deep > 8 km. Basically, shallow PFs contribute a very small fraction of the total precipitation (~5% from TRMM PR, ~2% from Revelle) throughout the MJO life cycle. Deep PFs produced the most rainfall (60-80%) during all MJO phases, with 20-40% of the rainfall contributed by PFs reaching heights at least to the mid-troposphere. Both TRMM PR and Revelle statistics show that deep PFs contribute 15-20% more rainfall in active periods than during MJO inactive periods (e.g., minimum at phases 5-6, and maximum at phase 2). This pattern of deep PF rainfall is exactly the same as that of MCS rainfall (Fig. 11). TRMM PR (70-85%, Fig. 12b) observed a higher fraction of rainfall originating from deep PFs compared to the Revelle radar (60-75%, Fig. 12c), as well as MCS rainfall (Fig. 11). As was previously discussed, TRMM PR tended to retrieve more rainfall (in the climatological sense) than the Revelle radar (Fig. 8) for MCSs of similar convective intensities (Fig. 7). The reasons for these differences remain unclear.

## 6. Conclusions

This study used 3-months of shipborne radar observations during the 2011-2012 DYNAMO field campaign along with a 15-yr climatology of TRMM PR measurements over the central Indian Ocean region to investigate convective morphologies, as well as convective intensity and rainfall contributions by each organizational category. This study first presented the convection/precipitation morphology characteristics of two major MJO events observed by the shipborne radar (Revelle radar) during DYNAMO. Time series of Revelle radar data indicated clear transitions of convective organization, intensity, and precipitation morphology from suppressed periods to active periods. The DYNAMO-based analysis was placed in the context of the substantially longer-term satellite (i.e., TRMM) climatology. This comparison indicates that the Revelle radar statistics are consistent with those from the long term TRMM PR record. Major findings in this study are as follows:

1) During the October and November 2011 MJO events observed by the Revelle radar, convective organization evolved from the sub-MCS organizational mode in suppressed periods to the MCS-dominated mode in active periods; this transition was consistent with those of the convective intensity and environmental conditions; MCSs were rare outside the MJO convective envelope;

2) The Revelle radar well captured major climatological characteristics of MJO convection as indicated by comparison to the long-term TRMM PR statistics over the DYANMO array, including aspects of areal mean rainfall (6-7 mm $d^{-1}$), distributions of convective intensities (20/30 dBZ echo-top heights), rainfall contributions from the four morphology categories, and variations of these parameters as a function of MJO phase;

3) Sub-MCSs (including both linear and non-linear) were present 90% of the time (20% in linear and 70% in non-linear mode), but only contributed roughly 30% of the total precipitation (10% in linear and 20% in non-linear mode); non-linear MCS events contribute much more volumetric rain (50%) compared to linear MCS events (20%), owing to their higher frequency of occurrence; however, these distributions also varied with MJO phase, with the highest sub-MCS rainfall fraction in suppressed phases (phases 5-7) and maximum MCS precipitation in active phases (phases 2-3);

4) Convective cells are deeper within MCSs (e.g. 20 and 30 dBZ echo-top heights are on average 2 km higher) compared to sub-MCSs; convective-stratiform rainfall fraction varies significantly with MJO phase, with the highest convective fraction (70-80%) in suppressed phases and the largest stratiform fractions (40-50%) in active phases; similarly, active phases are also characterized by maximum fraction of rainfall generated by deep convective cells;

5) There are differences between the statistics derived from Revelle radar and TRMM PR, such as convective/stratiform rainfall fraction (e.g., Revelle radar indicated a mean stratiform fraction of 30% compared to 45% for TRMM PR); TRMM PR composites indicate linear-MCS rainfall increases after MJO onset and produces similar rainfall contributions to non-linear MCSs; however, the Revelle radar statistics showed the clear dominance of non-linear MCS rainfall (more than twice that of linear-MCSs).

6) The TRMM PR estimated lower convective rain fractions compared to the Revelle radar. We suggest this is mainly due to the coarser resolution of the TRMM PR (4 km) relative to the Revelle radar (~2 km) such that the TRMM PR cannot adequately resolve various reflectivity gradients that are often characteristic of convection. When the Revelle radar data were degraded to 4 km resolution convective fractions between the two platforms were very similar.

# Acknowledgement:

This research was supported by the National Science Foundation DYNAMO Project grant AGS-1063928. We thank Edward Zipser and Chuntao Liu for providing the TRMM Precipitation Feature data. We also thank the entire crew of the R/V *Revelle* for their excellent support and *Revelle* Chief Scientist James Moum for his dedication and leadership. We are also grateful to Robert Houze, Courtney Schumacher, and Masaki Katsumata, and their research groups for data analysis and radar science discussions. We thank Ramesh Kakar, John Gerlach Walter Petersen and the late Arthur Hou (all NASA) for making the NASA TOGA radar available for DYNAMO. Chidong Zhang was the Lead PI for DYNAMO and we are grateful for his excellent leadership of the project.

# References

Alexander, G. D., and G. S. Young, 1992: The relationship be- tween EMEX mesoscale precipitation feature properties and their environmental characteristics. *Mon. Wea. Rev.,* **120,** 554–564.

Awaka, J., T. Iguchi, and K. Okamoto, 2009: TRMM PR standard algorithm 2A23 and its performance on bright band detection. *J. Meteor. Soc. Japan*, **87,** 31–52.

Barnes, G. M., and K. Seickman, 1984: The environment of fast- and slow-moving tropical mesoscale convective cloud lines. *Mon. Wea. Rev.,* **112,** 1782–1794.

Bechtold, P., M. Köhler, T. Jung, F. Doblas-Reyes, M. Leutbecher, M. J. Rodwell, F. Vitart, and G Balsamo, 2008: Advances in simulating atmospheric variability with the ECMWF model: From synoptic to decadal time-scales. *Quart. J. Roy. Meteor. Soc*., **134**, 1337–1351.

Bladé, I., and D. L. Hartmann, 1993: Tropical intraseasonal oscillations in a simple nonlinear model. *J. Atmos. Sci.*, **50**, 2922-2939.

Ciesielski, P. E, H. Yu, R. H. Johnson, K. Yoneyama, M. Katsumata, C. N. Long, J. Wang, S. M. Loehrer, K. Young, S. F. Williams, W. Brown, J. Braun, and T. Van Hove, 2014: Quality-controlled upper-air sounding dataset for DYNAMO/CINDY/AMIE: Development and corrections. *J. Atmos. Ocean. Tech.*, **in press**.

Cifelli, R., S. W. Nesbitt, S. A. Rutledge, W. A. Petersen, S. Yuter, 2007: Radar Characteristics of Precipitation Features in the EPIC and TEPPS Regions of the East Pacific. *Mon. Wea. Rev.*, **135**, 1576–1595

Cheng, C.-P and R.A. Houze Jr., (1979). The distribution of convective and mesoscale precipitation in GATE radar echo patterns. *Mon. Wea. Rev.*, **107**, 1370–1381.

Feng, Z., S. A. McFarlane, C. Schumacher, S. Ellis, J. Comstock, and N. Bharadwaj, 2014: Constructing A Merged Cloud-Precipitation Radar Dataset for Tropical Convective Clouds during the DYNAMO/AMIE Experiment at Addu Atoll. *J. Atmos. Tech.*, doi:10.1175/JTECH-D-13-00132.1, in press.

Gamache, J. F., and R. A. Houze, 1983: Water budget of a mesoscale convective system in the Tropics. *J. Atmos. Sci.,* **40,** 1835–1850.

Gottschalck, J., P.E. Roundy, C. J. Schreck III, A.Vintzileos, and C. Zhang, 2013: Large-scale atmospheric and oceanic conditions during the 2011-12 DYNAMO field campaign. *Mon. Wea. Rev.,* **141**, 4173–4196.

Guy, N., D. P. Jorgensen, 2014: Kinematic and Precipitation Characteristics of Convective Systems Observed by Airborne Doppler Radar during the Life Cycle of a Madden–Julian Oscillation in the Indian Ocean. *Mon. Wea. Rev.*, **142**, 1385–1402.

Hendon, H. H., and B. Liebmann, 1990: The intraseasonal (30– 50 day) oscillation of the Australian summer monsoon, *J. Atmos. Sci.*, **47**, 2909–2923.

Houze, R. A. Jr., 1977: Structure and dynamics of a tropical squall-line system. *Mon. Wea. Rev.*, **105**, 1540–1567.

Houze, R. A. Jr., and E. N. Rappaport, 1984: Air motions and precipitation struc- ture of an early summer squall line over the eastern tropical Atlantic. *J. Atmos. Sci.,* **41,** 553–574.

Houze, R. A., Jr., 1989: Observed structure of mesoscale convective systems and implications for large-scale heating. *Quart. J. Roy. Me- teor. Soc.,* **115,** 425–461.

Hu, Q. and D. A. Randall, 1994: Low-frequency oscillations in radiative-convective systems. *J. Atmos. Sci.*, **51**, 1089–1099.

Huffman, G. J., and Coauthors, 2007: The TRMM Multisatellite Precipitation Analysis (TMPA): Quasi-Global, Multiyear, Combined-Sensor Precipitation Estimates at Fine Scales. *J. Hydrometeor*, **8**, 38–55

Hung, M.-P., J.-L. Lin, W. Wang, D. Kim, T. Shinoda, and S. J. Weaver, 2013: MJO and convectively coupled equatorial waves simulated by CMIP5 climate models. J. Climate, **26**, 6185–6214.

Iguchi, T., T. Kozu, J. Kwiatkowski, R. Meneghini, J. Awaka, and K. Okamoto, 2009: Uncertainties in the rain profiling algorithm for the TRMM precipitation radar. *J. Meteor. Soc. Japan*, **87,** 1–30.

Johnson, R. H., 1984: Partitioning tropical heat and moisture bud- gets into cumulus and mesoscale components: Implications for cumulus parameterization. *Mon. Wea. Rev.,* **112,** 1590– 1601.

Johnson, R. H., T. M. Rickenbach, S. A. Rutledge, P. E. Ciesielski, and W. H. Schubert, 1999: Trimodal characteristics of tropical convection. *J. Atmos. Sci.*, **58**, 2729–2750.

Johnson, R. H., and P. E. Ciesielski, 2013: Structure and properties of Madden-Julian Oscillations deduced from DYNAMO sounding arrays. *J. Atmos. Sci.*, **70**, 3157-3179.

Kemball-Cook, S. R., and B. C. Weare, 2001: The onset of convection in the Madden-Julian oscillation. *J. Climate*, **14**, 780-793.

Kummerow, C., W. Barnes, T. Kozu, J. Shiue, J. Simpson, 1998: The Tropical Rainfall Measuring Mission (TRMM) Sensor Package. *J. Atmos. Oceanic Technol.*, **15**, 809–817

Kikuchi, K. and Y. N. Takayabu, 2004: The development of organized convection associated with the MJO during TOGA COARE IOP: Trimodal characteristics. *Geophys. Res. Lett.*, **31**, doi:10.1029/2004GL019601.

Keenan, T. D., and R. E. Carbone, 1992: A preliminary morphol- ogy of precipitation systems in tropical northern Australia. *Quart. J. Roy. Meteor. Soc.,* **118,** 283–326.

Kim, D., K. Sperber, W. Stern, D. Waliser, I.-S. Kang, E. Maloney, S. Schubert, W. Wang, K. Weickmann, J. Benedict, M. Khairoutdinov, M.-I. Lee, R. Neale, M. Suarez, K. Thayer-Calder, and G. Zhang, 2009: Application of MJO Simulation Diagnostics to Climate Models, *J. Climate*, **22**, 6413-6436.

Lawrence, D. M., and P. J. Webster, 2002: The boreal summer intraseasonal oscillation: Relationship between northward and eastward movement of convection, *J. Atmos. Sci.*, **59**, 1593-1606.

Lau, K.-M., and P. H. Chan, 1986: Aspects of the 40–50 day oscillation during the northern summer as inferred from outgoing longwave radiation, *Mon. Weather Rev.*, **114**, 1354–1367.

Lau, K.-M., and D. E. Waliser, 2005: Intraseasonal Variability in the Atmosphere-Ocean Climate System, 436 pp., *Praxis*, Chichester, U.K.

Lau, W.K.M., 2012: El – Niñ0 Southern Oscillation connection. Intraseasonal Variability of the Atmosphere–Ocean Climate System. 2nd Ed., W.K.M. Lau and D. E. Waliser, Eds., Springer, Heidelberg, Germany, 297-334.

Leary, C. A., 1984: Precipitation structure of the cloud clusters in a tropical easterly wave. *Mon. Wea. Rev.,* **112,** 313–325.

LeMone, M. A., 1983: Momentum transport by a line of cumulonimbus. *J. Atmos. Sci.,* **40,** 1815–1834.

LeMone, M. A., G. M. Barnes, and E. J. Zipser, 1984: Momentum flux by lines of cumulonimbus over the tropical ocean. *J. Atmos. Sci.,* **41,** 1914 –1932.

LeMone, M. A., E. J. Zipser, and S. B. Trier, 1998: The role of environmental shear and thermodynamic conditions in determining the structure and evolution of mesoscale convective systems dur- ing TOGA COARE. *J. Atmos. Sci.,* **55,** 3493–3518.

L'Heureux, Michelle L., R. Wayne Higgins, 2008: Boreal Winter Links between the Madden–Julian Oscillation and the Arctic Oscillation. J. Climate, 21, 3040-3050.

Liebmann, B., H. Hendon, and J. Glick, 1994: The relationship between tropical cyclones of the western Pacific and Indian oceans and the Madden-Julian Oscillation, *J. Meteorol. Soc. Jpn.*, **72**, 401–411.

Lau, K.-M., and H.-T. Wu, 2010: Characteristics of precipitation, cloud, and latent heating associated with the Madden–Julian oscillation. *J. Climate,* **23**, 504–518.

Lin H., G. Brunet, and J. Derome, 2009: An observed connection between the North Atlantic

Oscillation and the Madden-Julian Oscillation. J. Climate, 22, 364-380.

Lin, J.-L., G.N. Kiladis, B.E. Mapes, K.M. Weickmann, K.R. Sperber, W. Lin, M.C. Wheeler, S.D. Schubert, A. Del Genio, L.J. Donner, S. Emori, J.-F. Gueremy, F. Hourdin, P.J. Rasch, E. Roeckner, and J.F. Scinocca, 2006: Tropical intraseasonal variability in 14 IPCC AR4 climate models. Part I: Convective signals. *J. Climate*, **19**, 2665-2690.

Lin, J-L., and B. Mapes, 2004: Wind shear effects on cloud-radiation feedback in the western Pacific warm pool. *Geophys. Res. Lett.*, **31.**L16118, doi:10.1029/2004GL020199.

Lin, X., and R. H. Johnson (1996), Kinematic and thermodynamic characteristics of the flow over the western Pacific warm pool during TOGA COARE, *J. Atmos. Sci.*, **53**, 695 – 715.

Liu, C., and E. J. Zipser, D. J. Cecil, S. W. Nesbitt, and S. Sherwood, 2008: A cloud and precipitation feature database from nine years of TRMM observations, *J. Appl. Meteor.*, **47**, 2712-2728.

Liu, C., and E. Zipser, 2013: Regional variation of morphology of organized convection in the tropics and subtropics, *J. Geophys. Res. Atmos.*, **118**, 453–466, doi:10.1029/2012JD018409.

Madden, R. A., and P. R. Julian, 1971: Detection of a 40-50-day oscillation in the zonal wind in the tropical Pacific. *J. Atmos. Sci.*, **28**, 702-708.

Madden, R. A., and P. R. Julian, 1972: Description of global-scale circulation cells in the tropics with a 40-50 day period. *J. Atmos. Sci.*, **29**, 1109-1123.

Maddox, R. A. (1980). Mesoscale convective complexes, Bull. Am. Meteorol. Soc.. 61, 1374–1387.

Maloney, E. D., D. L. Hartmann, 1998: Frictional Moisture Convergence in a Composite Life Cycle of the Madden–Julian Oscillation. *J. Climate*, **11**, 2387–2403.

Maloney, E. D., and D. L. Hartmann, 2000: Modulation of eastern North Pacific hurricanes by the Madden-Julian Oscillation, *J. Climate*, **13**, 1451–1460.

Medioni, G., M.-S. Lee, and C. K. Tang, 2000: A Computational Framework for Segmentation and Grouping. Elsevier, 260 pp.

Moncrieff, M. W., and J. S. A. Green, 1972: The propagation and transfer properties of steady convective overturning in shear. *Quart. J. Roy. Meteor. Soc.,* **98,** 336–352.

Morita, J., Y. N. Takayabu, S. Shige, and Y. Kodama, 2006: Analysis of rainfall characteristics of the Madden–Julian oscillation using TRMM satellite data. *Dyn. Atmos. Oceans*, **42,** 107–126.

Moum, J. N., S. P. DeSzoeke, W. D. Smith, J. B. Edson, H. L. DeWitt, A. Moulin, E. J. Thompson, C. J. Zappa, S. A. Rutledge, R. H. Johnson and C. W. Fairall, 2014: Air-Sea interactions from the Westerly Wind Burst events during the November 2011 MJO in the Indian Ocean. *Bull. Amer. Meteor. Soc.*, In press.

Nesbitt, S. W., E. J. Zipser, D. J. Cecil, 2000: A Census of Precipitation Features in the Tropics Using TRMM: Radar, Ice Scattering, and Lightning Observations. *J. Climate*, **13**, 4087–4106.

Nesbitt, S. W., R. Cifelli, S. A. Rutledge, 2006: Storm Morphology and Rainfall Characteristics of TRMM Precipitation Features. *Mon. Wea. Rev.*, **134**, 2702–2721

Oye, D., and M. Case, 1995: REORDER: A program for gridding radar data. Installation and use manual for the UNIX version. *NCAR/ATD*, 30 pp.

Petersen, W. A., S. A, Rutledge and R. E. Orville, 1996: Cloud-to-Ground Lightning Observations from TOGA COARE: Selected Results and Lightning Location Algorithms. *Mon. Wea. Rev.*, **124**, 602-620.

Powell, S., and R. A. Houze. Jr., 2014: The cloud population and onset of the Madden-Julian Oscillation over the Indian Ocean during DYNAMO-AMIE. *J. Geophys. Res.*, **118**, 11,979–11,995, doi:10.1002/2013JD020421.

Rickenbach, T. M., S. A. Rutledge, 1998: Convection in TOGA COARE: Horizontal Scale, Morphology, and Rainfall Production. *J. Atmos. Sci.*, **55**, 2715–2729.

Riley, E. M., B. E. Mapes, and S. N. Tulich, 2011: Clouds associated with the Madden-Julian oscillation: A new perspective from cloudsat. *J. Atmos. Sci.*, **68**, 3032–3051.

Rowe, A. K. and R. A. Houze, Jr, 2014: Microphysical characteristics of MJO convection over the Indian Ocean during DYNAMO. *J. Geophys. Res. Atmos.*, **119**, 2543-2554 doi:10.1002/2013JD020799.

Saxen, T. R., S. A. Rutledge, 1998: Surface Fluxes and Boundary Layer Recovery in TOGA COARE: Sensitivity to Convective Organization. *J. Atmos. Sci.*, **55**, 2763–2781.

Short, D. A., P. A. Kucera, B. S. Ferrier, J. C. Gerlach, S. A. Rutledge, O. W. Thiele, 1997: Shipboard Radar Rainfall Patterns within the TOGA COARE IFA. *Bull. Amer. Meteor. Soc.*, **78**, 2817–2836.

Small, R. J., et al., 2008: Air-sea interaction over ocean fronts and eddies. *Dyn. Atmos. Oceans*, **45**, 274–319.

Szoke, E. J., and E. J. Zipser, (1986). A radar study of convective cells in mesoscale systems in GATE. Part II: life cycles of convective cells, *J. Atmos. Sci.*, **43**, 199–218.

Steiner, M., R. A. Houze, Jr., and S. E. Yuter, 1995: Climatological characterization of three-dimensional storm structure from operational radar and rain gauge data. *J. Appl. Meteor.*, **34**, 1978-2007.

Tao, W. K., J. Simpson, C-H. Sui, B. Ferrier, S. Lang, J. Scala, M-D. Chou, and K. Pickering, 1993: Heating, moisture, and water budgets of tropical and midlatitude squall lines: Comparisons and sensitivity to longwave radiation. *J. Atmos. Sci.*, **50,** 673–690.

Tromeur, E., and W. B. Rossow, 2010: Interaction of tropical deep convection with the large-scale circulation in the MJO. *J. Climate,* **23**, 1837–1853.

Thompson, D.B., and P.E. Roundy, 2012: The Relationship between the Madden-Julian Oscillation and U.S. Violent Tornado Outbreaks in the Spring. Mon. Wea. Rew., **141**, 2087–2095.

Thompson J. E., S. A. Rutledge, B. Dolan, M. Thurai, 2014: Long term 2DVD observations of rainfall characteristics in the Equatorial Indian and West Pacific Oceans. J. Atmos. Sci., submitted.

Tung, W.-W., and M. Yanai, 2002: Convective momentum trans- port observed during the TOGA COARE IOP. Part I: Gen- eral features. *J. Atmos. Sci.,* **59,** 1857–1871.

Vitart, F., and F. Molteni, 2010: Simulation of the Madden–Julian oscillation and its teleconnections in the ECMWF forecast system. *Quart. J. Roy. Meteor. Soc.*, **136**, 842–855.

Wheeler, M., and H. H. Hendon, 2004: An all-season real-time multivariate MJO index: Development of an index for monitor- ing and prediction. *Mon. Wea. Rev.*, **132**, 1917–1932.

Wu, X., and M. Yanai, 1994: Effects of vertical wind shear on the cumulus transport of momentum: Observations and param- eterization. *J. Atmos. Sci.,* **51,** 1640–1660.

Xie, S.-P., 2004: Satellite observations of cool oceanatmosphere interaction. *Bull. Amer. Meteor. Soc.*, **85**, 195–208.

Xu, W., and E. J. Zipser, 2012: Regime Variations among Continental, Monsoon, and Oceanic Deep Convection over the Tropics. *Geophys. Res. Lett.*, **39**, L07802, doi.10.1029/2012GL051242.

Xu, W. and S.A. Rutledge, 2014: Convective Characteristics of the Madden-Julian Oscillation over the Central Indian Ocean Observed by Shipborne Radar during DYNAMO. *J. Atmos. Sci.*, **71**, 2859-2877.

Yoneyama, K., C. Zhang, and C. N. Long, 2013: Tracking pulses of the Madden-Julian Oscillation, *Bull. Amer. Meteor. Soc.*, **94**, 1871–1891.

Zhang, C., 2005: Madden-Julian oscillation. *Rev. Geophys.*, **43**, RG2003, doi:10.1029/2004RG000158.

Zhang, C., 2013: Madden-Julian Oscillation: Bridging Weather and Climate. *Bull. Amer. Meteor. Soc.*, **94**, 1849–1870.

Zipser, E. J., (1977). Mesoscale and convective-scale downdraughts as distinct components of squall-line circulation. Mon. Wea. Rev., 105, 1568–1589.

Zipser, E. J., R. J. Meitin, and M. A. LeMone, 1981. Mesoscale motion fields associated with a slowly moving GATE convective band. *J. At- mos. Sci.,* **38,** 1725–1750.

Zipser, E. J., 1994: Deep Cumulonimbus Cloud Systems in the Tropics with and without Lightning. *Mon. Wea. Rev.*, **122**, 1837–1851.

Zuluaga, M. D., and R. A. Houze, Jr., 2013: Evolution of the population of precipitating convective systems over the equatorial Indian Ocean in active phases of the Madden-Julian oscillation. *J. Atmos. Sci.*, **70**, 2713–2725.

# Figure captions

**Figure 1.** Examples precipitation features (PFs, reflectivity > 17 dBZ at 2-km) observed by: (a) TRMM PR at 2251UTC 10/18 2011, (b) Revelle radar at 2250UTC 10/18 2011. Examples of different morphologies of PFs measured by Revelle radar: (c) Sub-L (sub-MCS linear), Sub-NL (sub-MCS nonlinear), and MCS-L (MCS linear) at 0300UTC 11/09 2011, and (d) MCS-NL (MCS Nonlinear) at 0000UTC 10/25 2011. PFs in (c)-(d) are fit into ellipses (dash line) for major axis and minor axis (solid line).

**Figure 2.** Rainfall distribution (TRMM 3B42) over the Indian Ocean as a function of WH MJO phase. (a)-(c): during MJO 1 (phase 1: 10/15 – 10/19, phase 2: 10/20-29, phase 3: 10/30-11/3, 2011), and (d)-(f) during MJO 2 (phase 1: 11/17-11/20, phase 2: 11/21-11/25, phase 3: 11/26-11/30, 2011). The DYNAMO array is marked by solid black line, while the white dashed box defines the climatology study region (75-85 E; 5 S- 5 N). DYNAMO radar ranges are marked by circles: Revelle radar (black solid), S-pol on Gan Is. (black dashed), and the C-band radar on R/V Mirai (black dashed).

**Figure 3.** Time series (3 hourly) of areal mean rainrate (based on Revelle radar) as a function of different morphologies: (a) during R/V Revelle cruise 2, and (b) during R/V Revelle cruise 3. Corresponding WH MJO phase numbers are indicated on the upper x-axis.

**Figure 4.** Cumulative distribution function (CDF) of PF population and rainfall fraction as a function of PF area. Revelle radar data (square) are from Oct. to Dec. in 2011, and TRMM PR data (star) are selected over (75-85 E; 5 S- 5 N) during Oct.-Apr. from 1998 to 2012.

**Figure 5.** Total PF frequency (green), fraction of total rain volume (blue), and convective rainfall fraction of different morphology categories: (a) statistics from Revelle radar, and (b) statistics based on TRMM PR. Error bars pass the T test at 95% confidence interval based on daily means.

**Figure 6.** The same as Fig. 5, but for (a) MIT radar statistics during TOGA COARE, and (b) TRMM PR statistics over the large TOGA COARE region (140-150 E; 5 S- 5 N) during 1998-2012 Oct.-Apr.

**Figure 7.** PDFs (probability distribution function) of PFs categorized by: (a) maximum 20 dBZ echo-top height and (b) maximum 30 dBZ echo-top height, based on Revelle radar (blue) and TRMM PR (red) measurements. Specific precipitation morphology of different categories are indicated by different markers.

**Figure 8.** CDFs (cumulative distribution function) of rain volumes contributed from different PFs categorized by: (a) maximum 20 dBZ echo-top height and (b) maximum 30 dBZ echo-top height, based on Revelle radar (blue) and TRMM PR (red) measurements. PFs of specific precipitation morphology are indicated by different markers.

**Figure 9.** Rainfall (areal mean) composites as a function of WH MJO phase from various rainfall estimation methods. Rainfall over the Revelle radar coverage area during October-December 2011 (when R/V Revelle was in station) is derived from the Revelle radar (black star) and TRMM 3B42 (orange dimond). TRMM 3B42 rainfall is also averaged over (5 S – 5 N; 75- 85 E) during October-December 2011 (blue triangle). Long-term (15-yr) TRMM PR (2A25) rainfall is averaged over (5 S – 5 N; 75- 85 E) during October-April from 1998-2012 (red square). Note that the 1:2:1 smooth filter has been applied to these time series. Error bars pass the T test at 95% confidence interval based on daily means.

**Figure 10.** Rainfall composites as a function of WH MJO phase contributed by convective and stratiform precipitation. (a)-(b): Revelle radar statistics, and (c)-(d): TRMM PR statistics.

**Figure 11.** Rainfall composites as a function of WH MJO phase contributed from PFs of different precipitation morphologies. (a)-(b): Revelle radar measurements, and (c)-(d): TRMM PR statistics.

**Figure 12.** Same as Fig. 11, but for rainfall contributed from PFs of different 20-dBZ echo heights: shallow (< 5 km), middle (between 5-8 km), and deep (> 8 km).

# Tables

**Table 1.** Rain depth (areal mean rainrate) during MJO wet periods of MJO 1 (10/14-10/29) and MJO 2 (11/15-11/30). Fractions of rainfall contributed from systems of specific morphology category are also listed.

| MJO Envelope | Rain depth (mm $d^{-1}$) | Linear MCS (%) | Non-linear MCS (%) | Linear sub-MCS (%) | Non-linear sub-MCS (%) |
|---|---|---|---|---|---|
| MJO 1 | 13.7 | 16 | 61 | 7 | 16 |
| MJO 2 | 9.3 | 15 | 49 | 11 | 25 |

**Table 2.** Summary of total PF population, areal mean rainrate, convective precipitation area percentage, convective rainfall fraction observed by TRMM PR and the Revelle radar. Areal mean rainrate derived from the TRMM 3B42 is listed in the bracket. Revelle radar data are from Oct.-Dec. 2011, and TRMM PR data are during Oct.-Apr. in 1998-2012 over (75-85 E; 5 S -5 N).

|  | Total PF Samples | Areal Mean Rainrate (mm/day) | Convective Area Fraction | Fraction of Convective Rain Volume |
|---|---|---|---|---|
| TRMM PR (3B42) | 87,140 | 6.1<br>(6.6) | 27% | 55% |
| Revelle Radar | 77,408 | 7.0 | 25% | 73% |

**Table 3.** Samples of MJO event days and PFs as a function of WH MJO phase in the TRMM PR and Revelle radar dataset. TRMM PR dataset includes measurements observed during Oct.-Apr. from 1998 to 2012 over the CIO (75-85 E; 5 S -5 N). TRMM sampling for WH MJO composites only include significant MJO days (i.e., $RMM1^2 + RMM2^2 > 1.2$).

| **Phase** | **1** | **2** | **3** | **4** | **5** | **6** | **7** | **8** |
|---|---|---|---|---|---|---|---|---|
| TRMM Sampling Days | 138 | 189 | 227 | 187 | 234 | 231 | 194 | 180 |
| TRMM PFs | 4749 | 6177 | 6006 | 3586 | 5173 | 5276 | 4996 | 5757 |
| Revelle Sampling Days | 9 | 14 | 5 | 10 | 6 | 6 | 8 | 9 |
| Revelle PFs | 12708 | 22043 | 6645 | 9453 | 1406 | 1371 | 3699 | 10538 |

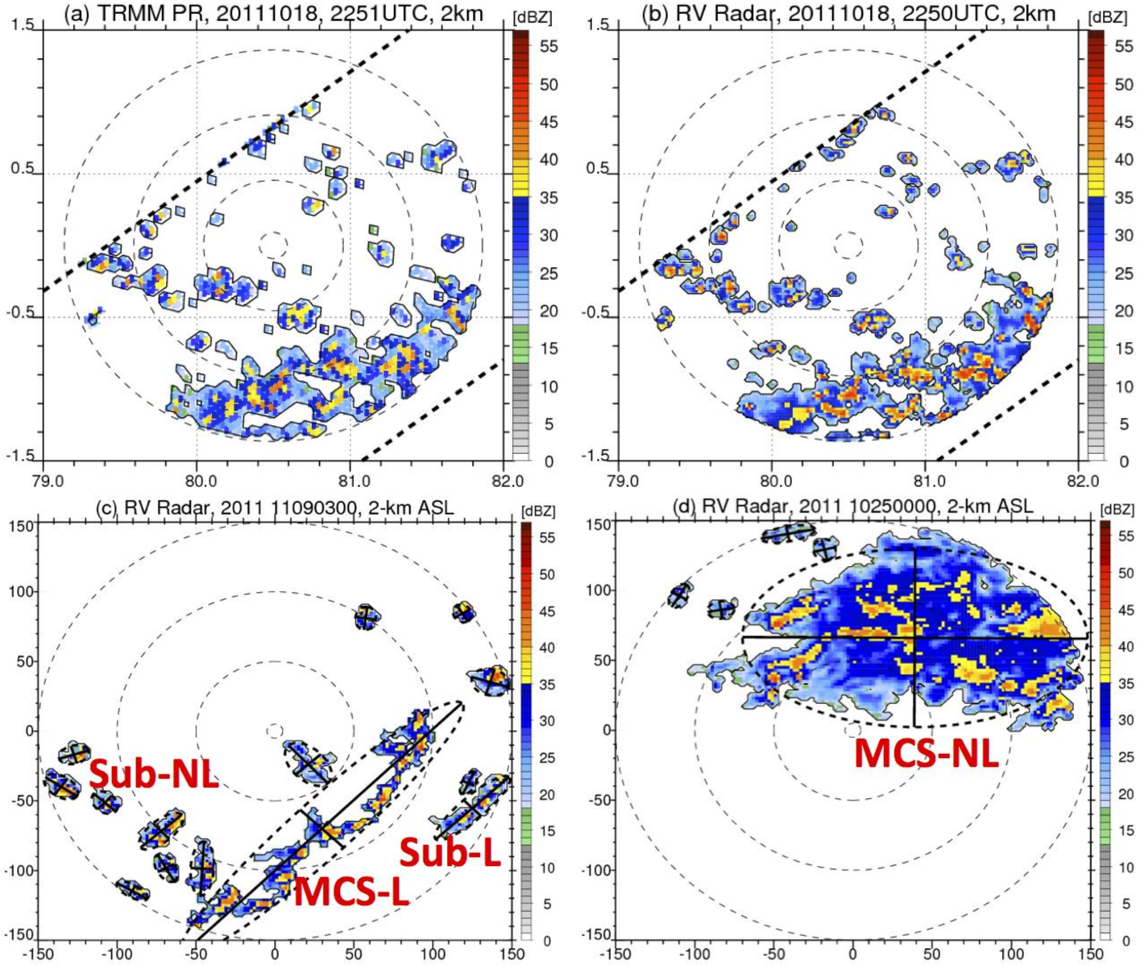

**Figure 1.** Examples precipitation features (PFs, reflectivity > 17 dBZ at 2-km) observed by: (a) TRMM PR at 2251UTC 10/18 2011, (b) Revelle radar at 2250UTC 10/18 2011. Examples of different morphologies of PFs measured by Revelle radar: (c) Sub-L (sub-MCS linear), Sub-NL (sub-MCS nonlinear), and MCS-L (MCS linear) at 0300UTC 11/09 2011, and (d) MCS-NL (MCS Nonlinear) at 0000UTC 10/25 2011. PFs in (c)-(d) are fit into ellipses (dash line) for major axis and minor axis (solid line).

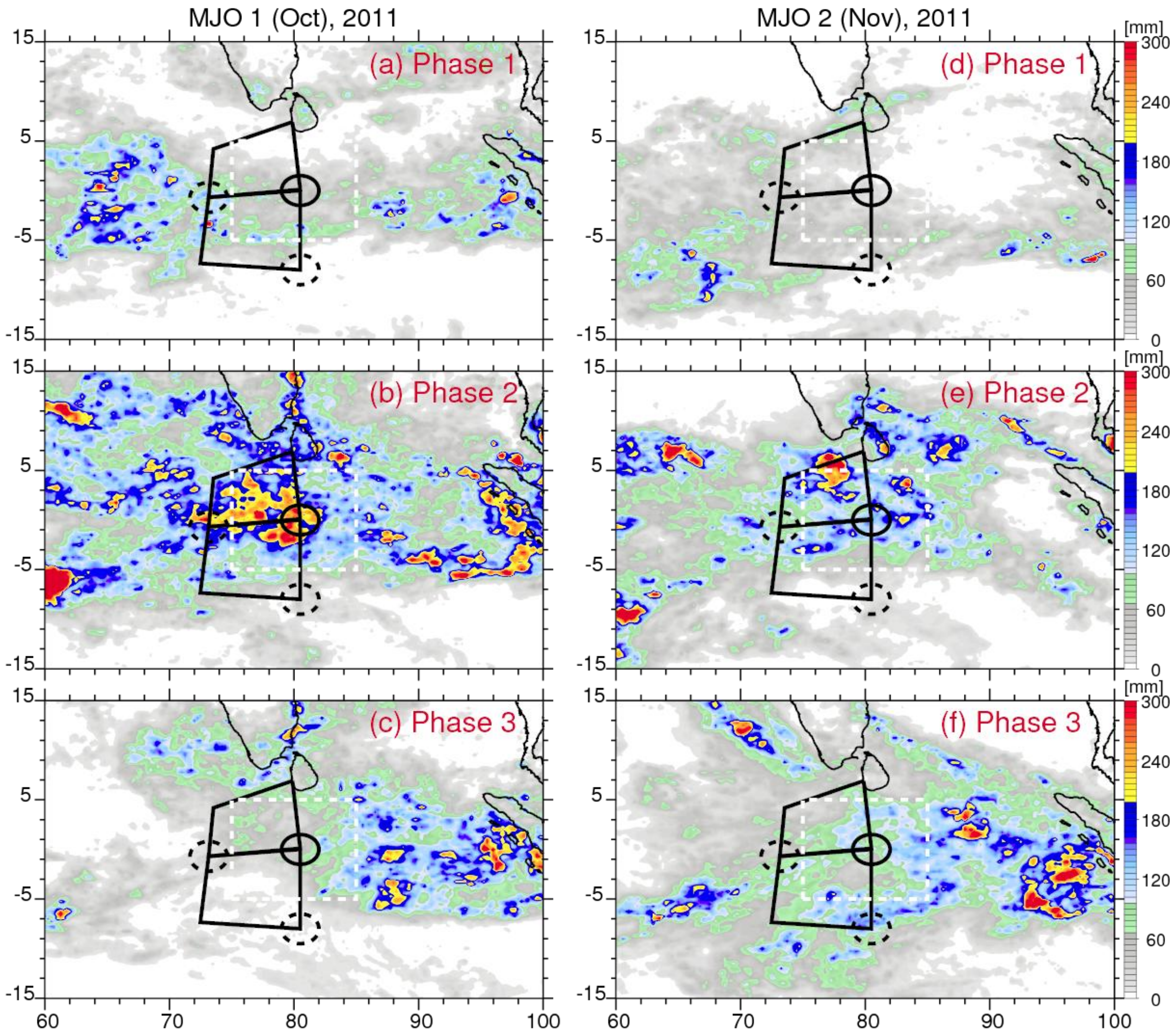

**Figure 2.** Rainfall distribution (TRMM 3B42) over the Indian Ocean as a function of WH MJO phase. (a)-(c): during MJO 1 (phase 1: 10/15 – 10/19, phase 2: 10/20-29, phase 3: 10/30-11/3, 2011), and (d)-(f) during MJO 2 (phase 1: 11/17-11/20, phase 2: 11/21-11/25, phase 3: 11/26-11/30, 2011). The DYNAMO array is marked by solid black line, while the white dashed box defines the climatology study region (75-85 E; 5 S- 5 N). DYNAMO radar ranges are marked by circles: Revelle radar (black solid), S-pol on Gan Is. (black dashed), and the C-band radar on R/V Mirai (black dashed).

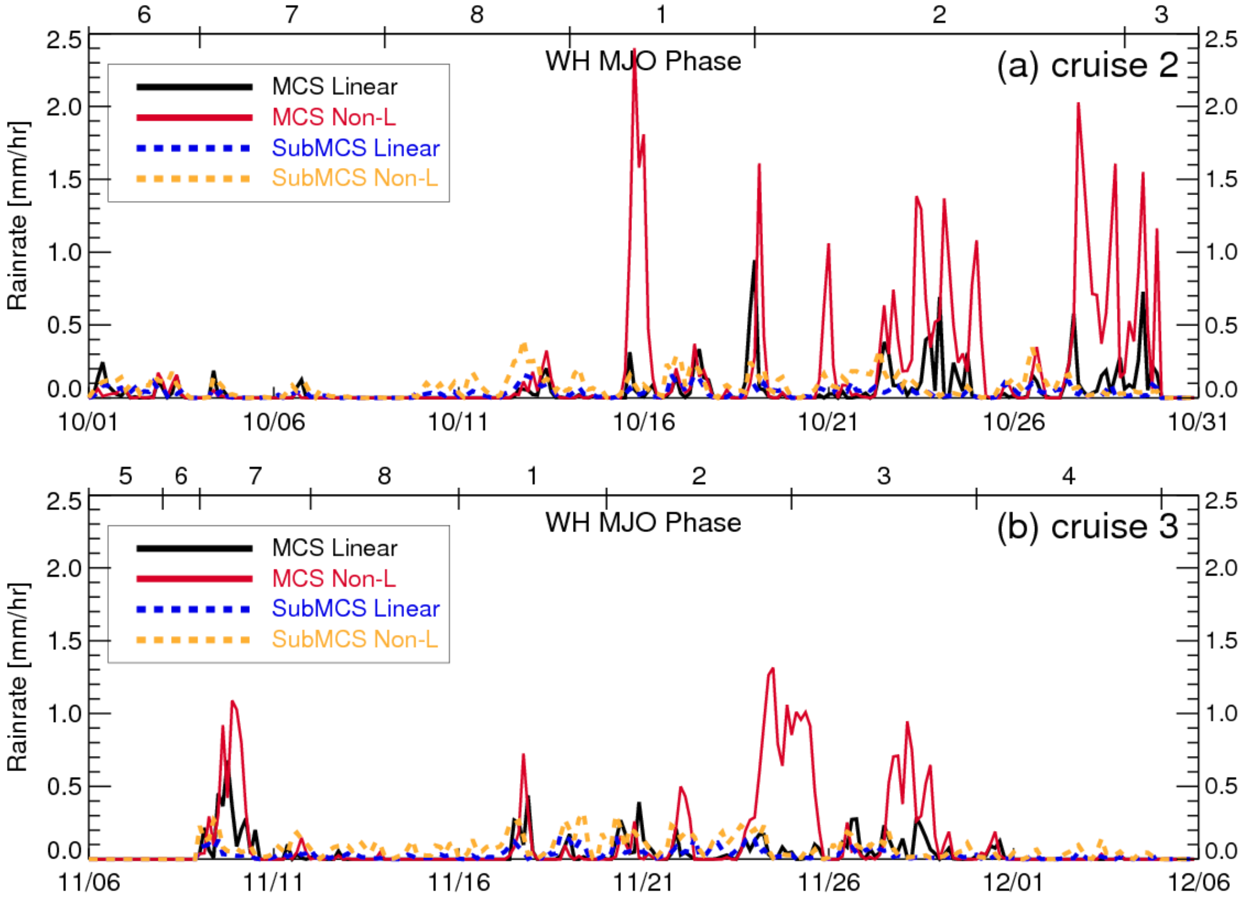

**Figure 3.** Time series (3 hourly) of areal mean rainrate (mm hr$^{-1}$) as a function of different morphologies during R/V Revelle: (a) cruise 2, and (b) cruise 3. Corresponding WH MJO phase numbers are indicated on the upper x-axis.

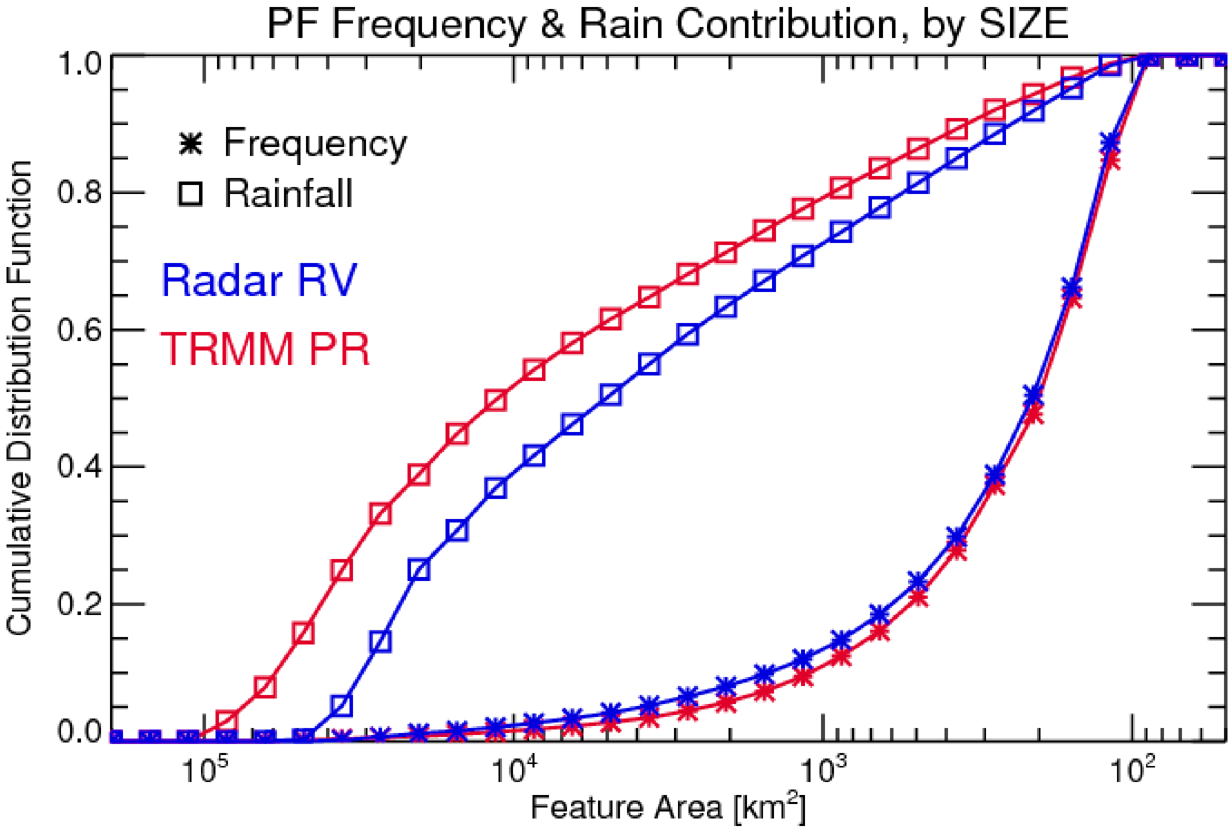

**Figure 4.** Cumulative distribution function (CDF) of PF population and rainfall fraction as a function of PF area. Revelle radar data are from Oct. to Dec. in 2011, and TRMM PR data are selected over (75-85 E; 5 S- 5 N) during Oct.-Apr. from 1998 to 2012.

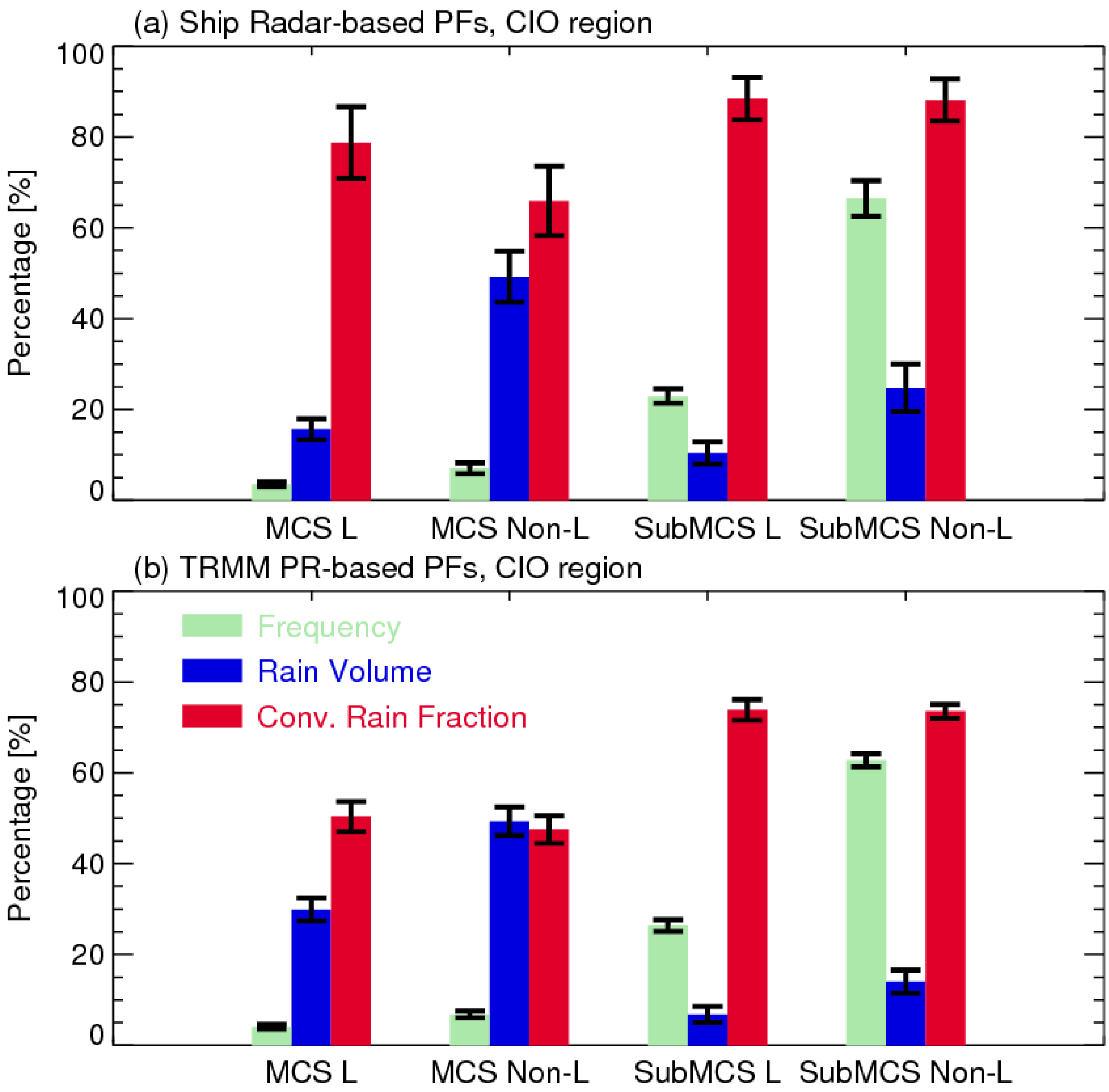

**Figure 5.** Total PF frequency (green), fraction of total rain volume (blue), and convective rainfall fraction of different morphology categories: (a) statistics from Revelle radar, and (b) statistics over (75-85 E; 5 S- 5 N) based on TRMM PR. Error bars pass the T test at 95% confidence interval based on daily means.

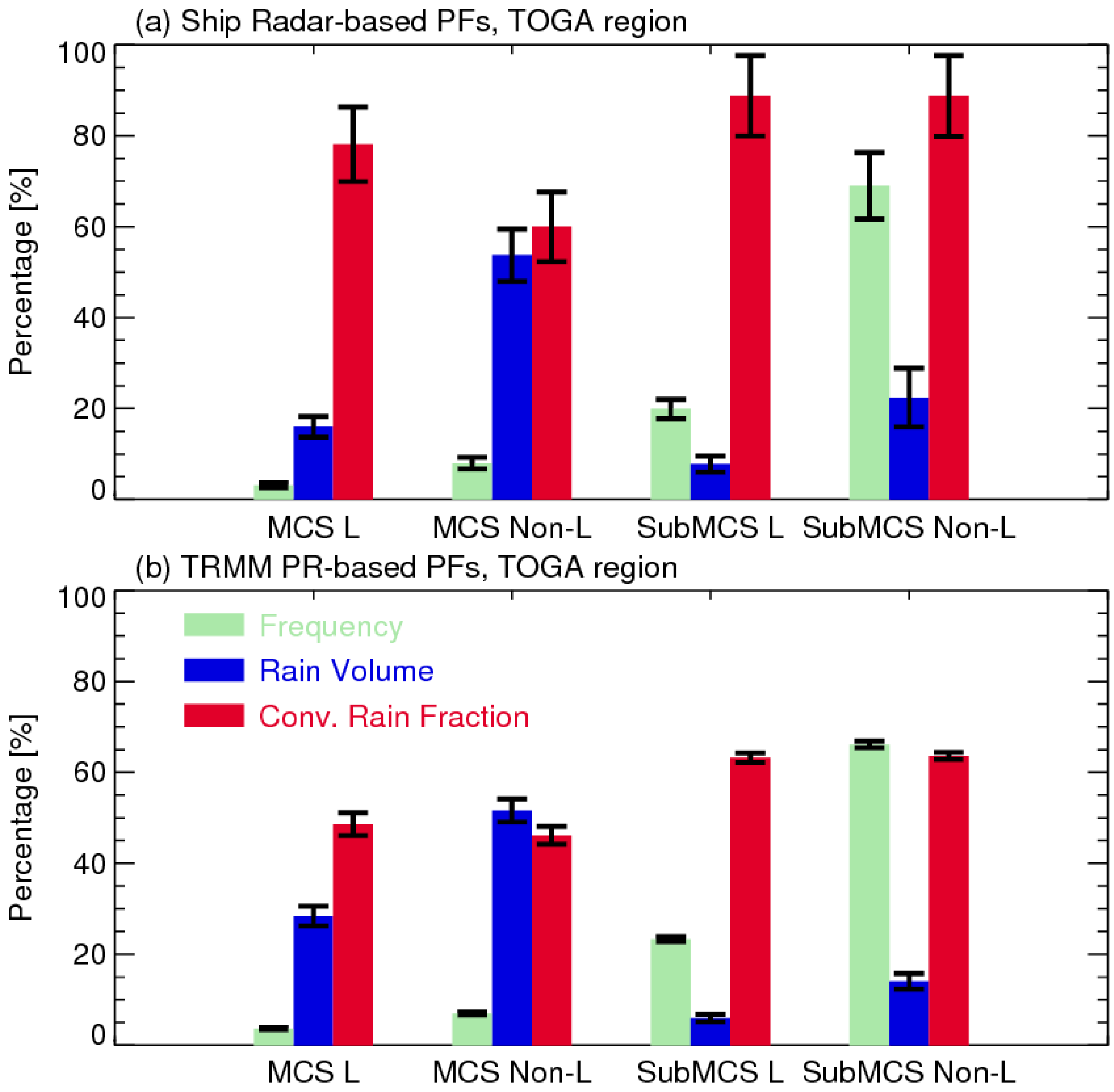

**Figure 6.** The same as Fig. 5, but for (a) MIT radar statistics, and (b) TRMM PR statistics over the large TOGA COARE region (140-150 E; 5 S- 5 N).

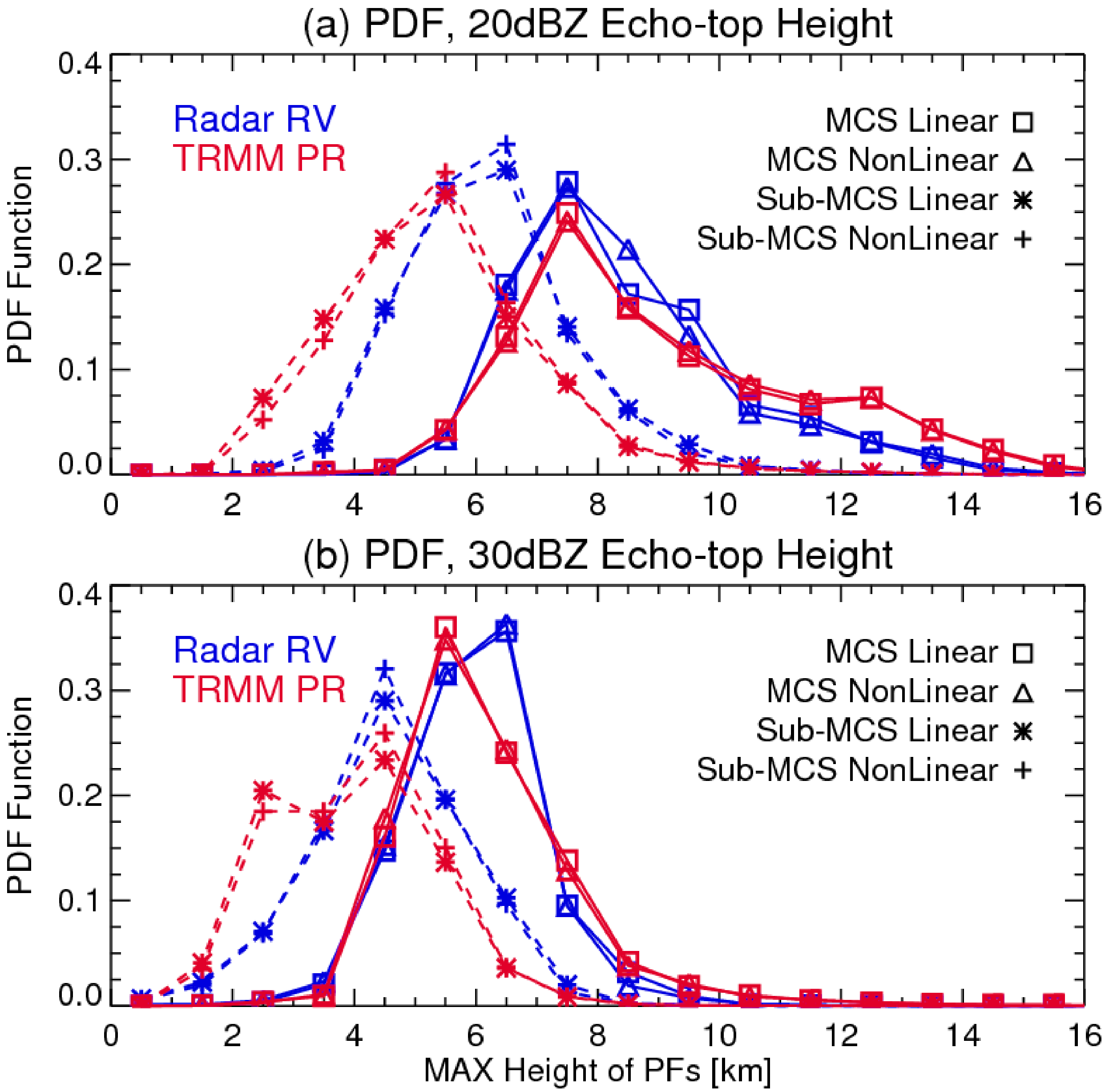

**Figure 7.** PDFs (probability distribution function) of PFs categorized by: (a) maximum 20 dBZ echo-top height and (b) maximum 30 dBZ echo-top height, based on Revelle radar (blue) and TRMM PR (red) measurements. Specific precipitation morphology of different categories are indicated by different markers.

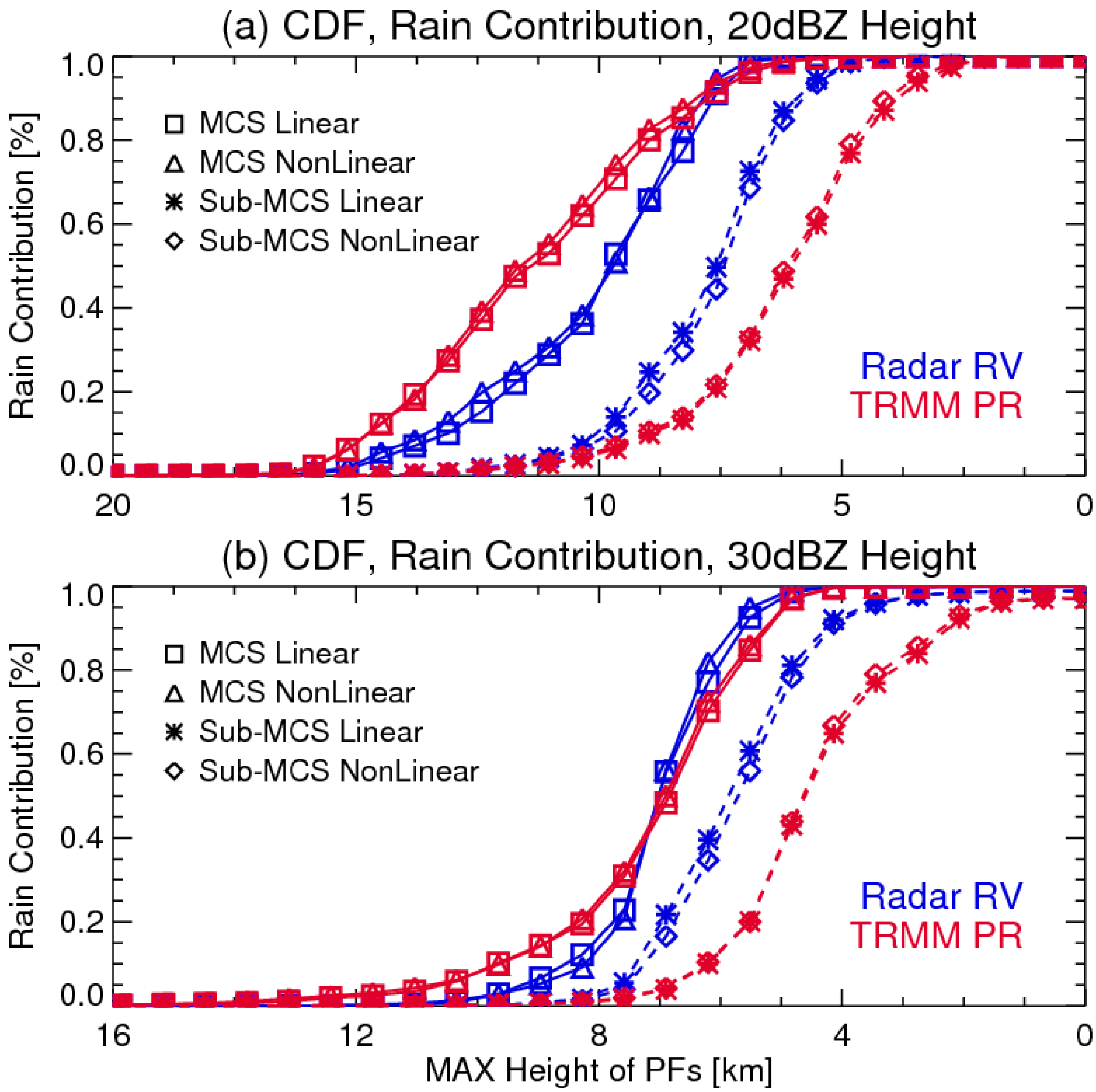

**Figure 8.** CDFs (cumulative distribution function) of rain volumes contributed from different PFs categorized by: (a) maximum 20 dBZ echo-top height and (b) maximum 30 dBZ echo-top height, based on Revelle radar (blue) and TRMM PR (red) measurements. PFs of specific precipitation morphology are indicated by different markers.

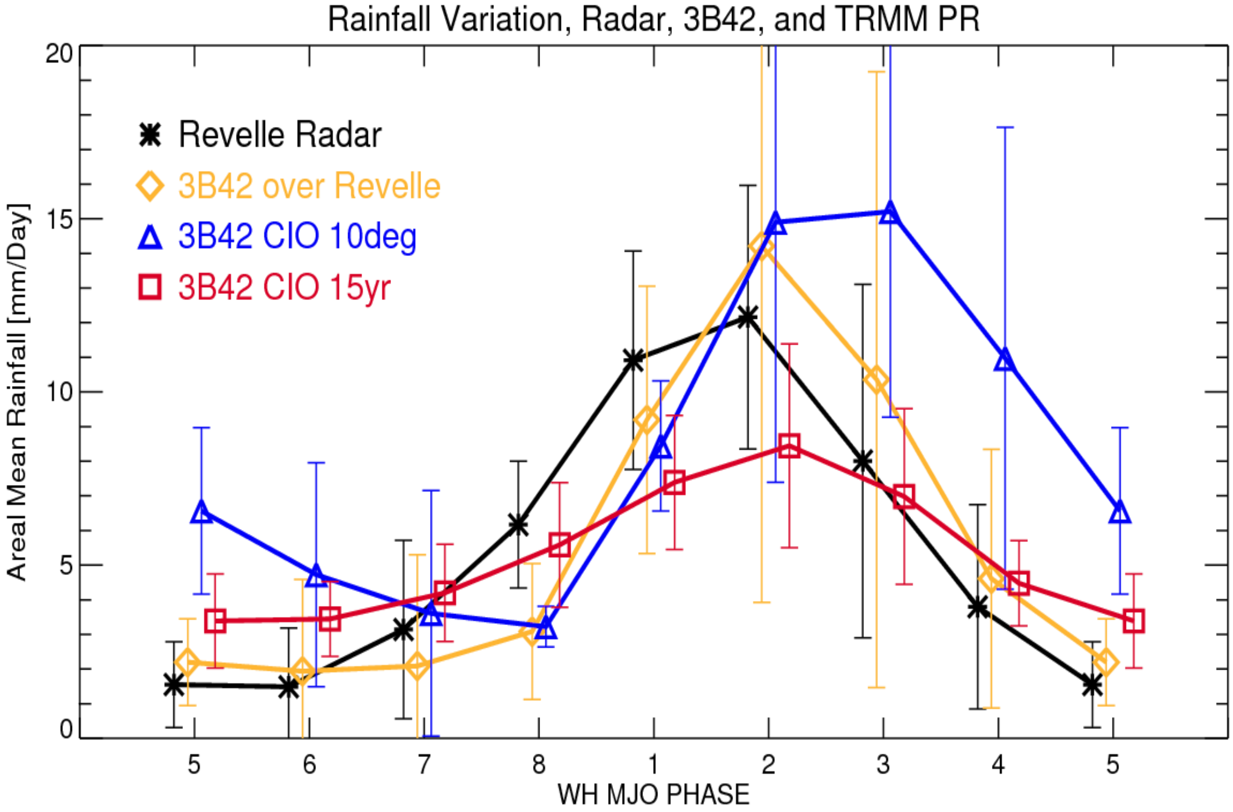

**Figure 9.** Rainfall composites as a function of WH MJO phase from various rainfall estimation methods. Rainfall over the Revelle radar coverage area during October-December 2011 is derived from the Revelle radar (black star) and TRMM 3B42 (orange dimond). TRMM 3B42 rainfall is also averaged over (5 S – 5 N; 75- 85 E) during October-December 2011 (blue triangle). Long-term (15-yr) TRMM PR (2A25) rainfall is averaged over (5 S – 5 N; 75- 85 E) during October-April from 1998-2012 (red square). Note that the 1:2:1 smooth filter has been applied to these time series. Error bars pass the T test at 95% confidence interval based on daily means.

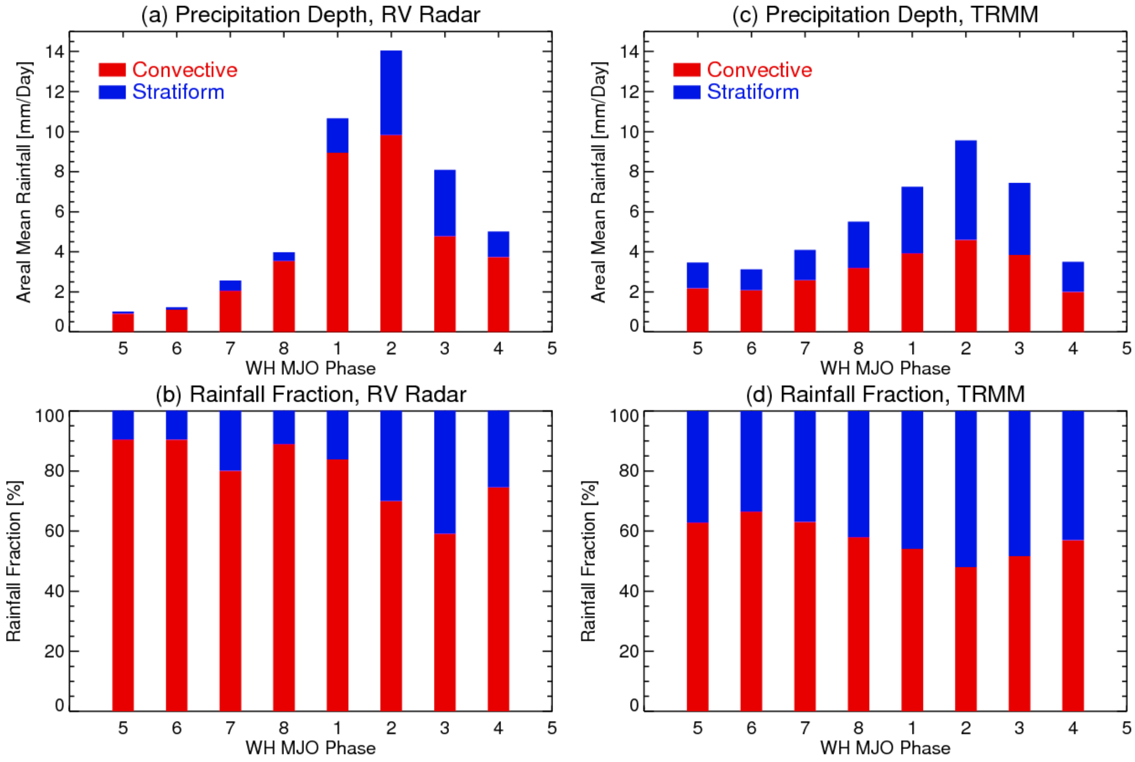

**Figure 10.** Rainfall composites as a function of WH MJO phase contributed by convective and stratiform precipitation. (a)-(b): Revelle radar statistics, and (c)-(d): TRMM PR statistics.

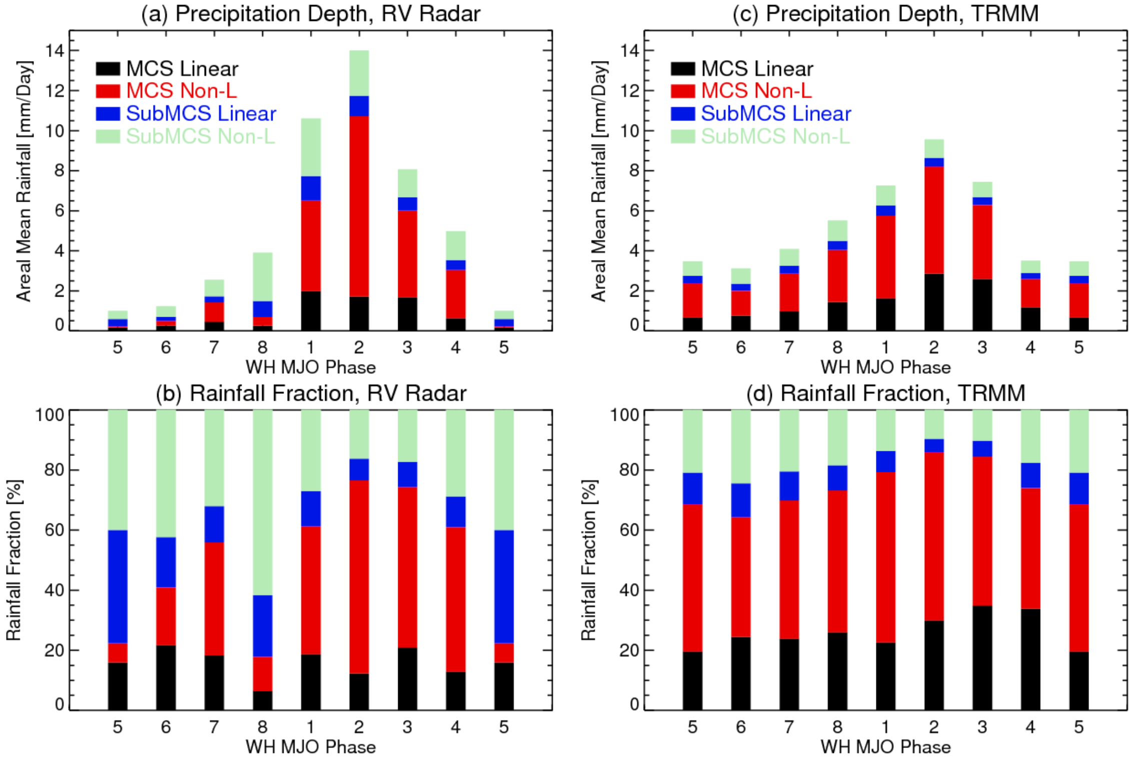

**Figure 11.** Rainfall composites as a function of WH MJO phase contributed from PFs of different precipitation morphologies. (a)-(b): Revelle radar measurements, and (c)-(d): TRMM PR statistics.

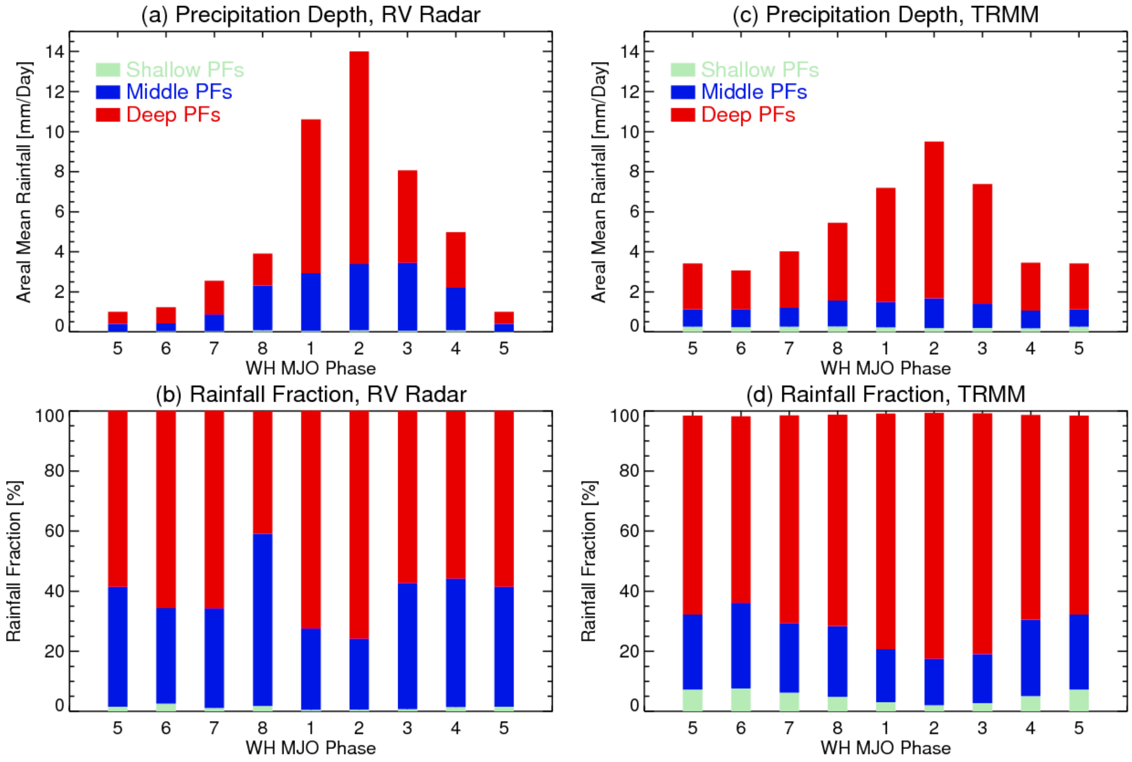

**Figure 12.** Same as Fig. 11, but for rainfall contributed from PFs of different 20-dBZ echo heights: shallow (< 5 km), middle (between 5-8 km), and deep (> 8 km).